PHYSICAL REVIEW RESEARCH **4**, 013242 (2022)

Unified Green's function approach for spectral and thermodynamic properties from algorithmic inversion of dynamical potentials

Tommaso Chiarotti,[1,*] Nicola Marzari,[1] and Andrea Ferretti[2]
[1]*Theory and Simulations of Materials (THEOS) and National Centre for Computational Design and Discovery of Novel Materials (MARVEL), École Polytechnique Fédérale de Lausanne, 1015 Lausanne, Switzerland*
[2]*Centro S3, CNR–Istituto Nanoscienze, 41125 Modena, Italy*

(Received 11 August 2021; accepted 21 January 2022; published 29 March 2022)

Dynamical potentials appear in many advanced electronic-structure methods, including self-energies from many-body perturbation theory, dynamical mean-field theory, electronic-transport formulations, and many embedding approaches. Here, we propose a novel treatment for the frequency dependence, introducing an algorithmic inversion method that can be applied to dynamical potentials expanded as sum over poles. This approach allows for an exact solution of Dyson-like equations at all frequencies via a mapping to a matrix diagonalization, and provides simultaneously frequency-dependent (spectral) and frequency-integrated (thermodynamic) properties of the Dyson-inverted propagators. The transformation to a sum over poles is performed introducing nth order generalized Lorentzians as an improved basis set to represent the spectral function of a propagator. Numerical results for the homogeneous electron gas at the G_0W_0 level are provided to argue for the accuracy and efficiency of such unified approach.

DOI: 10.1103/PhysRevResearch.4.013242

I. INTRODUCTION

Electronic-structure calculations have been and remain a powerful and ever expanding field of research to understand and predict materials properties [1]. The development of methods, algorithms, and hardware brings in continuous progress, allowing for computational materials discovery [2–4], accurate comparison with experiments [5,6], and even hybrid quantum-computation algorithms [7,8].

Due to the interaction between the electrons in a system, solving the many-body quantum problem is often at the core of many approaches. Focusing on condensed-matter systems, density-functional theory (DFT) has been one of the most used and successful methods so far [9]. The possibility to map exactly the ground-state solution of the N-body problem to the minimization of a density functional for the energy [10] offers great computational simplifications, allowing for the accurate computation of ground-state quantities for most materials. Although mathematically well defined [11] and computationally inexpensive, it remains challenging to improve on existing approximate functionals [12,13]—often resulting in incorrect predictions for complex or strongly-correlated systems [14]—or to address spectroscopic properties [15,16].

Dynamical, i.e., frequency-dependent, approaches like many-body perturbation theory, dynamical mean-field theory, and in general embedding schemes offer the flexibility to overcome these limitations of DFT. While the theoretical framework differs in different approaches, a common element is the appearance of dynamical potentials. As an example, many-body perturbation theory (MBPT) reduces the multiparticle electronic degrees of freedom to a single particle subjected to a nonlocal and dynamical potential, the electron-electron self-energy [17]. Dynamical mean-field theory (DMFT) couples a real-space impurity with the rest of the system, requiring self-consistency between the impurity and the bath [18–20]. Coherent electronic-transport theories use a Green's function embedding to calculate the electronic conductance of, e.g., a conductor between two semi-infinite leads, coupling the three systems dynamically [21,22]. Clearly, handling properly frequency-dependent potentials is of central interest in the field.

Using MBPT as a paradigmatic example, we highlight that the difficulty in treating dynamical quantities has often led to different methodological approaches when calculating spectral or thermodynamic quantities (such as energies, number of particles, chemical potentials). Real-axis calculations are commonly performed to compute the frequency-dependent spectral properties [23–25], while the frequency-integrated thermodynamic properties are typically calculated using an imaginary-axis formalism [26–31]. The difference in the two approaches originates from the analytic structure of the Green's function and specifically from its branch cuts on the real axis [32]. This results in the spectral function—related to the imaginary part of a Green's function—strongly varying for real frequencies and difficult to integrate on the real domain. Thus, real-axis approaches are often limited to the predictions of spectral properties. Conversely, sampling the Green's function along the imaginary axis, i.e., away from its poles, is a good way to obtain fast converging frequency integrals, but has drawbacks when trying to get the function on the real axis

---

[*] Corresponding author: tommaso.chiarotti@epfl.ch

by analytic continuation. In this context, methods to perform the analytic continuation range from the use of Padè approximants [31,33–35] to maximum-entropy methods [36,37], in this latter case usually with a stochastic sampling of the Green's function. As an example, in a recent paper on the homogeneous electron gas [38], Kutepov *et al.* [34] managed to get a precise quasiparticle band using Padè approximants (though with larger error bars on the position of satellites). Also, in a series of papers [39–42] von Barth and coworkers have proposed a formalism able to tackle spectra and thermodynamics together for the homogeneous electron gas, by modeling the spectral function in frequency-momentum space using Gaussians with k-parametrized centers (quasiparticle energies), broadening (weights), and satellites. Nevertheless due to its model nature, the approach does not easily offer the flexibility to target realistic systems and or extend to embedding problems in general.

In this paper we introduce a novel approach, termed algorithmic-inversion method, applied on sum-over-pole representations (AIM-SOP), to address the simultaneous calculation of accurate spectral and thermodynamic quantities. Within AIM-SOP, dynamical (frequency-dependent) self-energies are represented on sum over poles, and the exact solution—at all frequencies—of the Dyson equation is found via a matrix diagonalization. The transformation of a frequency-dependent propagator into a SOP via a representation of its spectral function on a target basis set is greatly improved with the introduction of nth order generalized Lorentzians as a basis with fast decay properties. The SOP form allows one to compute analytically convolutions and moments of propagators for the calculation of spectral, and thermodynamic properties. Owing to the fulfillment of all sum rules implied by the Dyson equation, we show that the AIM-SOP method becomes key to have accurate frequency-integrated quantities in a real-axis (thus, spectral oriented) formalism. As a case study, we consider the paradigmatic case of the homogeneous electron gas (HEG), for r_s from 1 to 10, treated at the G_0W_0 level [43–45].

The paper is organized as follows: In Sec. II we introduce the AIM-SOP approach, discussing its main goal, and the SOP form for propagators and self-energies. In Sec. II A we provide an overview of the connection between a propagator and its spectral function, first for a continuum and then extending it to treat spectral functions represented on discrete basis sets, that will be exploited in this paper. Then, we consider different basis sets to represent the spectral function and obtain a SOP representation introducing nth order Lorentzians. In Sec. II B we provide the numerical procedure to transform a propagator sampled on a grid to a SOP representation, and viceversa. In Sec. II C we introduce several useful expressions when dealing with propagators on SOP, such as analytic convolutions and moments. In Sec. II D we present the algorithmic-inversion method on sum over poles to obtain exact solutions on SOP of any Dyson-like equation. First, we provide a mathematical proof for the case of a self-energy on SOP, then we extend it to treat the Dyson equation for the polarizability, and finally we give a numerical example as proof-of-concept for the procedure. In Sec. II E we show with a numerical example the representation on SOP for a test propagator. In Sec. III we discuss the application of the method to the test case of the homogeneous electron gas. In Sec. IV we discuss the results obtained applying the AIM-SOP to the homogeneous electron gas at the G_0W_0 level, first treating the $r_s = 4$ case in detail and then presenting results for r_s from 1 to 10. Finally, in Sec. V we draw the conclusions for the paper. Technical aspects of the method are further presented in the Appendices.

II. METHOD: AIM-SOP FOR DYNAMICAL POTENTIALS

In this section we introduce the algorithmic-inversion method to treat dynamical (frequency-dependent) potentials. The crucial goal for AIM-SOP is to solve exactly and at all frequencies Dyson-like equations for dynamical potential expressed as sum over poles. For this purpose we express frequency-dependent propagators and self-energies (or, say, polarizabilities or screened Coulomb interactions) in a SOP form:

$$G(\omega) = A_0 + \sum_{i=1}^{N} \frac{A_i}{\omega - z_i}, \tag{1}$$

where the constant term A_0 may be present for self-energies and potentials. Generally, we consider here having complex residues A_i and poles $z_i = \epsilon_i + i\delta_i$ ($\epsilon_i, \delta_i \in \mathbb{R}$). Having $\delta_i \gtrless 0$ when $\epsilon_i \lessgtr \mu$ provides the correct time-ordered analytical structure, with μ the effective chemical potential of the propagator (for a Green's function μ is the Fermi energy of the system, for a polarizability or a screened potential $\mu = 0$). Here, N is the number of poles and it has to be treated as a convergence parameter. This is well discussed in Ref. [46], where the authors show that time-ordered propagators can always be written as a continuous fraction, for which the SOP representation with a finite N corresponds to a truncation. The procedure to choose a representative SOP for a given propagator—i.e., number of poles, poles, and amplitudes—is the subject of the next sections.

Throughout this paper we will focus on the homogeneous electron gas (HEG), where, due to translational symmetry, all the two-point operators (including Green's functions, self-energies, and polarizabilities) are diagonal on the plane-wave basis. The notation is chosen accordingly.

A. Spectral representations

Following Ref. [40], we consider the spectral representation of a propagator (here the Green's function for simplicity), where G is expressed in terms of its spectral function A,

$$G(\omega) = \int_{\mathcal{C}} \frac{A(\omega')}{\omega - \omega'} d\omega' \tag{2}$$

by performing a time-ordered Hilbert transform (TOHT), with $\mathcal{C}$ a time-ordered contour, which is shifted above/below the real axis for $\omega' \lessgtr \mu$, and where the shift is sent to zero after the integral is computed. Accordingly, the inverse relation to go from G to A is given by:

$$\begin{aligned} A(\omega) &= \frac{1}{2\pi i}[G(\omega) - G^{\dagger}(\omega)]\,\mathrm{sgn}(\mu - \omega) \\ &= \frac{1}{\pi}\mathrm{Im}G(\omega)\,\mathrm{sgn}(\mu - \omega), \end{aligned} \tag{3}$$

the last expression being valid for a scalar Green's function, as is the case for the HEG. Furthermore, by representing the spectral function on a (finite) basis set $\{b_j(\omega)\}_{1,\dots,M}$,

$$A(\omega) = \sum_{j=1}^{M} a_j b_j(\omega)\,\mathrm{sgn}(\mu - \epsilon_j) = \sum_{j=1}^{M} a_j |b_j(\omega)|, \tag{4}$$

with $b_j(\omega)$ centered on ϵ_j and positive (negative) for $\epsilon_j \lessgtr \mu$, and $a_j > 0$, we can induce a representation of G. This is achieved by introducing a discrete time-ordered Hilbert transform (D-TOHT) as

$$G(\omega) = \sum_{j=1}^{M} a_j \int \frac{|b_j(\omega')|}{\omega - \omega' - i0^+\,\mathrm{sgn}(\mu - \epsilon_j)}\, d\omega', \tag{5}$$

where the sign chosen for b_j in Eq. (4) gives by construction the time-ordered analytic structure of the Green's function. In the case of all b_j becoming Dirac delta functions and M infinitely large (continuum representation limit), Eq. (5) becomes the standard TOHT of Eq. (2) (with $\mathcal{C}$ shifted by $\pm i0^+$).

A natural choice is to use a basis of Lorentzian functions centered at different frequencies ϵ_j, according to

$$|b_j(\omega)| = \mathcal{L}_{\delta_j}(\omega - \epsilon_j) = \frac{1}{\pi}\frac{|\delta_j|}{(\omega - \epsilon_j)^2 + \delta_j^2}, \tag{6}$$

for which the D-TOHT for the single element is analytical, yielding a pole function $1/(\omega - z_j)$ with $z_j = \epsilon_j + i\delta_j$, with the sign convention for δ_j defined as in Sec. II. Thus, choosing b_j as in Eq. (6) induces a SOP representation for G according to Eq. (1), with $A_i = a_i \in \mathbb{R}$, and $N = M$. Once the SOP representation of G is known, i.e., poles and amplitudes are known, the grid evaluation (inverse of the above) is trivial and amounts to performing the finite sum in Eq. (1). This approach ensures a full-frequency treatment of the propagator (approaching the continuum representation limit when Lorentzians becomes delta functions), while preserving an explicit knowledge of the analytical structure and continuation of G.

One drawback of using Lorentzians to represent G is related to the slowly decaying tails ($1/\omega^2$ for $\omega \to \infty$) induced in the spectral function when using finite broadening values δ_j. In order to improve on this, we introduce here nth order generalized Lorentzians to obtain fast-decay basis functions. These are defined as

$$|b_j(\omega)| = \mathcal{L}^n_{\delta_j}(\omega - \epsilon_j) = \frac{1}{N_n \pi}\frac{|\delta_j|^{2n-1}}{(\omega - \epsilon_j)^{2n} + (\delta_j)^{2n}}, \tag{7}$$

where $N_n = [n \sin(\frac{\pi}{2n})]^{-1}$ is the normalization factor (see Appendix A). The D-TOHT of $\mathcal{L}^n_\delta$ remains analytic and still yields a SOP representation for G (see Appendix A):

$$\int_{\mathcal{C}} d\omega' \frac{\mathcal{L}^n_{\delta_j}(\omega' - \epsilon_j)}{\omega - \omega' - i0^+\,\mathrm{sgn}(\mu - \epsilon_j)} = \sum_{m=0}^{n-1} \frac{\alpha_m}{\omega - \zeta_{j,m}}, \tag{8}$$

with residues α_m and poles $\zeta_{j,m}$ given by

$$\alpha_m = \frac{1}{iN_n n} e^{i\frac{\pi}{2n}(1+2m)}, \tag{9}$$

$$\zeta_{j,m} = \epsilon_j + e^{i\frac{\pi}{2n}(1+2m)}\delta_j. \tag{10}$$

Importantly, α_m are complex [and so become the residues $A_i = a_j \alpha_m$ in the SOP representation of Eq. (1), i being a combined index], and $N = M \times n$. Thus, the spectral function of this SOP has contribution by both the real and the imaginary part of each Lorentzian pole $1/(\omega - \zeta_{j,m})$, resulting in an overall decay faster than each single Lorentzian. Also, it is worth noting that, as for standard Lorentzians, a normalized nth order Lorentzian approaches a Dirac delta for $\delta_j \to 0^+$.

Owing to their fast decay and to this last property, using a SOP for G_0 in terms of nth Lorentzians provides a faster convergence for $\delta \to 0^+$, in comparison with a SOP representation built on ordinary Lorentzians. While the use of nth order generalized Lorentzians to represent the spectral function $A(\omega)$ guarantees a faster decay in the imaginary part of the propagator, it results in a multiplication of the number of poles in the SOP for G (by the degree of the Lorentzian), and in having complex residues. As it will be shown in Sec. II C, the decay properties are fundamental for evaluating the moments of a SOP representation, assuring absolute convergence up to order $2(n-1)$. Also, the use of faster decay basis elements when representing the spectral function improves on the stability of the representation procedure, e.g., reducing the off-diagonal elements of the overlap matrix of the basis (see Sec. II B for details).

Alternatively to nth order Lorentzians, one could consider, e.g., using Gaussian functions to represent $A(\omega)$, and consequently $G(\omega)$, as done in Refs. [39,40]. Gaussians also allow for an analytical expression of the D-TOHT, at the price, though, of invoking the Dawson [47] or Faddeeva [48] functions to evaluate the real part of the propagator. Because of this, SOP expressions are not available, and basic operations involving propagators (such as those described in Sec. II C) cannot be performed analytically and need to be worked out in other ways, e.g., numerically or recasting the propagator expressions in term of spectral functions [39]. Furthermore, the algorithmic inversion technique, discussed in Sec. II D, is not available when using Gaussians basis sets to describe $A(\omega)$.

B. Transform to a sum over poles

Once the SOP representation has been introduced, the next important step is to determine numerically the SOP coefficients A_i and z_i in Eq. (1), given an evaluation of G on a frequency grid. According to the discussion of Sec. II A, the SOP representation can be seen equivalently as a representation for the Green's function G or for the spectral function A.

As a first case, we consider representing $A(\omega)$ according to Eq. (4), using the basis of nth order generalized Lorentzians introduced in Eq. (7). First, we define centers and broadening of the nth Lorentzians. Then, we obtain the coefficients a_j of the representation by performing a non-negative-least-square (NNLS) fit [48,49], thus assuring the positivity of all a_j. Finally, we use Eqs. (9) and (10) to get the SOP representation for the propagator. While the position and broadening (ϵ_j, δ_j) of the nth order Lorentzians could also be optimized by means of a nonlinear NNLS fit, here we consider them centered at $\epsilon_j = \frac{1}{2}(\omega_j + \omega_{j-1})$ and broadened with $\delta_j = |\omega_j - \omega_{j-1}|$, and we just linearly optimize a_j. Also, for numerical reasons we prefer to work with the bare imaginary part of G, i.e., without imposing the sign factor of Eq. (3), since this function is smoother than the actual spectral function $A(\omega)$ close to the Fermi level.

Alternatively, one could consider the basis representation induced on G via Eq. (1) in order to directly obtain the A_i and z_i coefficients (residues and poles). As for $A(\omega)$, this can be achieved by a linear or nonlinear LS fit (or interpolation) taking advantage of the knowledge of the whole $G(\omega)$ on a frequency grid (and not just of A). Interestingly, the SOP representation in Eq. (1) is a special case of a Padè approximant, written as the ratio of polynomials of order $N-1$ and N, respectively. Because of this, one can exploit Padè-specific approaches to determine (A_i, z_i), such as, for instance, Thiele's recursive scheme [50]. We found that this leads to a very efficient method when few tens of poles are considered, becoming numerically unstable beyond. For a recent exploitation of Padè and related techniques in the context of GW using a multipole approximation see Ref. [35]. Moreover, since the residues are not constrained to be real and positive (A_i are actually complex), there is no control over the time-ordered position of the poles, and the procedure is nontrivial to extend to the case of nth order Lorentzians. For the above reasons, in the present paper we adopt the first approach, based on the representation of $A(\omega)$.

C. Analytical expressions

Once the SOP representation of a dynamical propagator is available, a number of analytical expressions hold. For instance, the convolution of propagators, e.g., those involved in the evaluation of RPA-type polarizabilities or GW-like self-energies, can be directly evaluated using Cauchy's residue theorem:

$$\begin{aligned}\int_{-\infty}^{+\infty} \frac{d\omega'}{2\pi i}\, G(\omega+\omega')\tilde{G}(\omega')d\omega' &= \sum_{i,j}\int_{-\infty}^{+\infty} \frac{d\omega'}{2\pi i}\, \frac{A_i}{\omega+\omega'-z_i}\, \frac{\tilde{A}_j}{\omega'-\tilde{z}_j} \\ &= \sum_{\substack{i,j\\ \mathrm{Im}\{z_i\}<0\\ \mathrm{Im}\{\tilde{z}_j\}>0}} \frac{A_i\tilde{A}_j}{\omega+\tilde{z}_j-z_i} - \sum_{\substack{i,j\\ \mathrm{Im}\{z_i\}>0\\ \mathrm{Im}\{\tilde{z}_j\}<0}} \frac{A_i\tilde{A}_j}{\omega+\tilde{z}_j-z_i}. \end{aligned} \tag{11}$$

Using the the SOP for G, the following integrals can also be computed explicitly:

$$\begin{aligned} E_m[G] &= \oint_\Gamma \frac{dz}{2\pi i} e^{iz0^+} z^m G(z) \\ &= \sum_{\substack{i\\ \mathrm{Im}\{z_i\}>0}} A_i z_i^m, \end{aligned} \tag{12}$$

where we refer to the term $E_m[G]$ as the mth (regularized) moment of G. Γ here is a closed contour in the upper-half complex plane including the real axis plus the enclosing arc. We note that for the $m=0$, $m=1$, and $m=2$ moments, Γ can be reduced to the real axis using the $1/\omega$ decay of G (the symmetry of the integration domain is also invoked for $m=2$ to discard odd terms). In addition, in Appendix B we show that using an nth order Lorentzian basis to represent $G(\omega)$ on SOP, guarantees the first $2(n-1)$ regularized moments to coincide with the moments of the occupied spectral function of G, $\int_{-\infty}^{\mu} d\omega\, \omega^{2(n-1)} A(\omega)$.

D. Algorithmic inversion on SOP

As anticipated in the introduction, within the SOP approach the exact solution at all frequencies of the Dyson equation can be remapped into the diagonalization of a static effective Hamiltonian (Hermitian only under special conditions), a procedure that we refer to as "algorithmic-inversion method on sum over poles" (AIM-SOP); this is a central result for the present paper. As for the rest of the paper, we focus on the HEG—where all operators are complex-valued functions over frequency—and leave the treatment of the nonhomogeneous case to later work. Suppressing then the k momentum index for simplicity, let us suppose to have the SOP representation for the self-energy $\Sigma(\omega)$ and for the noninteracting Green's function $G_0(\omega)$ given by

$$\Sigma(\omega) = \sum_{i=1}^{N} \frac{\Gamma_i}{\omega-\sigma_i}, \qquad G_0 = \frac{1}{\omega-\epsilon_0}, \tag{13}$$

where any static part of the self-energy has been adsorbed in ϵ_0 for simplicity. Taking advantage of these expressions, the Dyson equation can be rewritten as

$$\begin{aligned} G(\omega) &= \left[G_0^{-1}(\omega) - \Sigma(\omega)\right]^{-1} \\ &= \frac{1}{\omega-\epsilon_0-\Sigma(\omega)} \\ &= \frac{(\omega-\sigma_1)\cdots(\omega-\sigma_N)}{T_N(\omega)}, \end{aligned} \tag{14}$$

in which the $N+1$ roots of the polynomial

$$\begin{aligned} T_N(\omega) = (\omega-\epsilon_0)\prod_{i=1,N}(\omega-\sigma_i) \\ - \sum_{j=1,N}\Gamma_j \prod_{\substack{i=1,N\\ i\neq j}}(\omega-\sigma_i) \end{aligned} \tag{15}$$

are the $N+1$ poles of the Green's function (as expected when the self-energy has N poles). The key statement of this section is that the roots of T_N can be obtained as the eigenvalues of the $(N+1)\times(N+1)$ matrix

$$H_{\mathrm{AIM}} = \begin{pmatrix} \epsilon_0 & \sqrt{\Gamma_1} & \dots & \sqrt{\Gamma_N} \\ \sqrt{\Gamma_1} & \sigma_1 & 0 & 0 \\ \vdots & 0 & \ddots & 0 \\ \sqrt{\Gamma_N} & 0 & \dots & \sigma_N \end{pmatrix}. \tag{16}$$

We prove this statement by observing that the characteristic polynomial of H_{AIM} is $T_N(\omega)$ via induction. Since the $N=1$ case is trivial we move to the Nth case. Using the Laplace expansion on the last line, the characteristic polynomial of the

Nth case can be written as

$$
\begin{aligned}
p_{H_{\mathrm{AIM}}}(\omega) &= \begin{vmatrix} \omega-\epsilon_0 & -\sqrt{\Gamma_1} & \dots & -\sqrt{\Gamma_N} \\ -\sqrt{\Gamma_1} & \omega-\sigma_1 & 0 & 0 \\ \vdots & 0 & \ddots & 0 \\ -\sqrt{\Gamma_N} & 0 & \dots & \omega-\sigma_N \end{vmatrix} \\
&= (\omega-\sigma_N)T_{N-1}(\omega) + (-1)^N\sqrt{\Gamma_N} \\
&\quad\times \begin{vmatrix} -\sqrt{\Gamma_1} & \dots & -\sqrt{\Gamma_{N-1}} & -\sqrt{\Gamma_N} \\ \omega-\sigma_1 & 0 & 0 & 0 \\ 0 & \ddots & 0 & 0 \\ 0 & \dots & \omega-\sigma_{N-1} & 0 \end{vmatrix}
\end{aligned}
\tag{17}
$$

where we have used the induction hypotheses in the first term of the right-hand side (rhs). Applying the same procedure to the last column of the second term, and making use of the definition in Eq. (15), we obtain

$$
\begin{aligned}
p_{H_{\mathrm{AIM}}}(\omega) &= (\omega-\sigma_N)T_{N-1}(\omega) - \Gamma_N \prod_{i=1,N-1}(\omega-\sigma_i) \\
&= T_N(\omega),
\end{aligned}
\tag{18}
$$

which completes the proof.

Calling z_i the poles of G, we calculate the residues by equating

$$
G(\omega) = \sum_{i=1}^{N+1} \frac{A_i}{\omega - z_i} = \frac{(\omega-\sigma_1)\cdots(\omega-\sigma_N)}{(\omega-z_1)\cdots(\omega-z_{N+1})},
\tag{19}
$$

and performing the limit $\lim_{\omega\to z_i}(\omega-z_i)$ on both sides (Heaviside cover-up method [51]), we obtain:

$$
A_i = \frac{\prod_{k=1}^{N}(z_i-\sigma_k)}{\prod_{j=1,\, j\neq i}^{N+1}(z_i-z_j)}.
\tag{20}
$$

We have thus proven that by knowing $\Sigma(\omega)$ represented on SOP, the SOP expression for G can be found by the diagonalization of the AIM-SOP matrix H_{AIM} from Eq. (16) followed by the evaluation of the residues using Eq. (20).

It is worth noting that the H_{AIM} matrix can be made Hermitian under special conditions. This happens, e.g., when we solve the Dyson equation for the retarded/advanced case in which the self-energy has poles with the same imaginary part $\mp\delta$, real and positive residues, and an equal broadening $\mp\delta$ for G_0 is assumed. Then, it is possible to include the imaginary part of the poles in the frequency variable ω, and solve the Dyson equation on the resulting complex path γ' (shifted by $\mp\delta$), yielding a symmetric H_{AIM}. After having found the SOP for G on γ', to have $G(\omega \in \mathcal{R})$ we analytically continue the solution to the real axis, obtaining $\mathrm{Im}\{z_i\} = \mp\delta$ for the retarded $(-)$ or advanced $(+)$ case.

We also stress that, given a self-energy represented on SOP, the solution provided by the algorithmic-inversion procedure is exact at all frequencies. This ensures that the Green's function fulfills all the sum-rules implied by the Dyson equation, including, e.g., the normalization of the spectral weight, and the first and second moment sum rules of the spectral function derived in Ref. [39]. This result is crucial when evaluating frequency-integrated quantities of a Green's function, such as the number of particles or the total energy (see Sec. III B).

Besides the solution of the Dyson equation for G, the AIM-SOP can also be used to solve the Dyson equation for the screened Coulomb interaction $W(\omega)$,

$$
\begin{aligned}
W(\omega) &= v_c + v_c P(\omega) W(\omega) \\
&= \frac{1}{1 - v_c P(\omega)} v_c = \epsilon^{-1}(\omega) v_c,
\end{aligned}
\tag{21}
$$

i.e., to compute the SOP representation of $W(\omega)$ once a SOP for the irreducible polarizability $P(\omega)$ is provided. Here v_c is the Coulomb potential (recalling that we are suppressing the momentum dependence for simplicity). By letting $P(\omega) = \sum_i \frac{S_i}{\omega - g_i}$, we can write:

$$
\begin{aligned}
\omega v_c P(\omega) &= \sum_i \omega \frac{v_c S_i}{\omega - g_i} \\
&= v_c \sum_i S_i + \sum_i \frac{v_c g_i S_i}{\omega - g_i} \\
&:= c_0 - C(\omega),
\end{aligned}
\tag{22}
$$

and following Eq. (21) (multiplied by $\frac{\omega}{\omega}$) we have

$$
\epsilon^{-1}(\omega) = \frac{1}{1 - v_c P(\omega)} = \frac{\omega}{\omega - c_0 - C(\omega)},
\tag{23}
$$

for which the AIM-SOP matrix can be used to find the poles of $\epsilon^{-1}(\omega)$ and $W(\omega)$. The amplitudes of W are easily found using Eq. (20), where we note that Eq. (19) has to be modified taking into account the frequency-constant shift of W by v_c, i.e., substituting $W(\omega) - v_c$ to G. Note that by multiplying ϵ^{-1} by $\frac{\omega}{\omega}$ in Eq. (23) we have inserted an extra zero in the denominator (at $\omega = 0$), which we need to discard from the eigenvalues of the AIM matrix [before applying the residue formula of Eq. (20)], since it simplifies with the ω factor at the numerator of Eq. (23). Consequently P, ϵ^{-1}, and W have all the same number of poles, at variance with the solution of the Dyson equation for G, where the number of poles of G is increased by one with respect to Σ.

As a numerical test for the AIM-SOP, we consider the Dyson equation for G within the example of a time-ordered self-energy built with 8 poles, as shown in the upper panel of Fig. 1 (the single pole of G_0 is not reported). In the lower panel we compare the Green's function G obtained from the numerical Dyson inversion on grid—done evaluating Σ on grid, and then inverting—against the Green's function found with the algorithmic inversion and evaluated on the frequency grid. The results are identical at the precision of the calculated eigenvalues of the AIM-SOP matrix, since the amplitude calculation of Eq. (20) is typically very well conditioned. This procedure has been tested in cases where hundreds of poles are used for the self-energy, without any numerical instabilities. It is important to note that the algorithmic-inversion method presented here shares similarities with procedures described in Refs. [52] and [53], also aimed at solving Dyson-like equations with a non-trivial frequency structure of the corresponding kernels.

E. Numerical validation of the transformation on sum over poles

We consider a target propagator G with a spectral function $A(\omega) = g_1(\omega) + \frac{1}{5}g_1(\omega+4) + \frac{1}{3}g_1(\omega-5)$, where $g_\sigma(\omega)$ is a

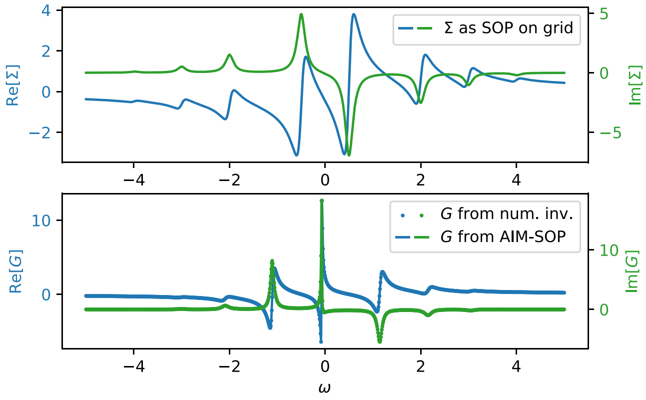

FIG. 1. Numerical example for the algorithmic inversion method on sum over poles. Upper panel: Real (blue) and imaginary (green) part of a time-ordered self-energy, having a SOP with 8 poles (the occupied pole of G_0 is not shown). Lower panel: Dyson-inverted propagator G obtained with a numerical inversion on a grid (dotted) compared with the SOP representation obtained using the algorithmic-inversion method and evaluated on the same grid (solid line). The same color code for real and imaginary parts as in the upper panel is used.

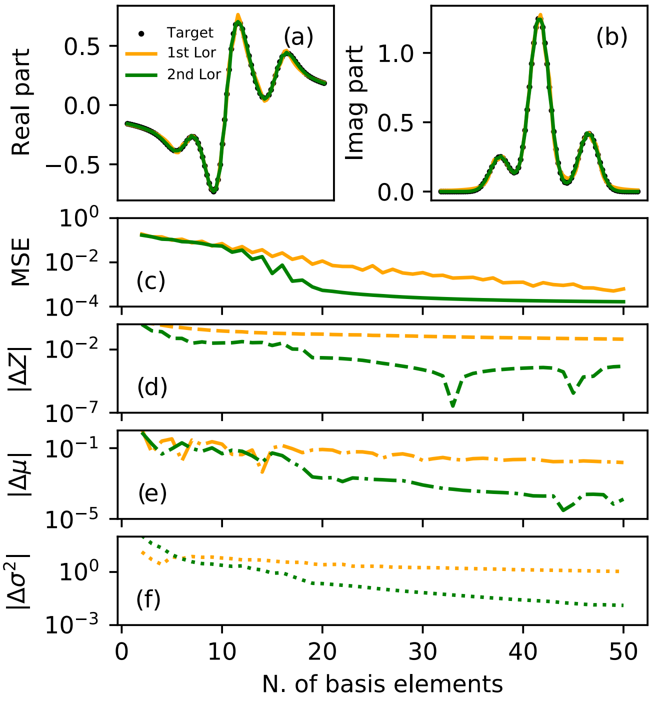

FIG. 2. Numerical example of a transformation to a SOP form. The target propagator is chosen to have a spectral function as a linear combination of three Gaussians, sampled using 50 points (black dots). We represent the trial spectral function on 1st (orange) and 2nd (green) order Lorentzian basis elements—each centered on the midpoint between adjacent grid points and broadened with the size of the interval—and get real and imaginary parts of the propagator analytically afterward (see Sec. II B for details). We plot the result in the panels (a) and (b). In panel (c) we study the mean-square error (MSE) of the fitted propagator against the target as a function of the number of basis elements used for the representation. The last value on this graph represents the MSE of the (sum of the) panels (a) and (b) between the fitted and the target values. All the other points in panel (c) are obtained placing the Lorentzians uniformly in the given interval with a broadening equal to the distance between two consecutive functions. In the panels (d)–(f) the same study is repeated for the absolute difference between the normalization of the target function and the one of the fitted propagator, its mean, and its variance. The y scales of the graphs (c)–(f) are logarithmic.

normalized Gaussian centered in zero and with variance σ^2. The propagator G can be obtained using the expression of the Faddeeva function [48], assuming the Fermi level to be far enough from the imaginary part of G, such that the retarded HT can be used. The goal of the validation is to best represent the target G as a sum over poles and compare the results obtained using 1st and 2nd order Lorentzian basis elements. We also study the mean-square error of the SOP-represented G as compared to the exact G, as a function of the number of poles used for the SOP, together with the absolute error of the mean and variance.

Following Sec. II B, we represent the spectral function A via a NNLS fit on 1st (ordinary) and 2nd order Lorentzian basis, and use Eqs. (9) and (10) to get the SOP for G. Here we use nth Lorentzian centered on a equally spaced grid with a broadening equal to the distance between two subsequent centers. In the panels (a) and (b) of Fig. 2 we adopt 50 basis elements to represent the target G sampled on 50 points. The real (panel a) and imaginary (panel b) parts of the target propagator are represented as black dots. The continuous lines represent the SOP obtained for G using 1st order (orange) and 2nd order (green) Lorentzian basis elements. Qualitatively it is possible to see that 2nd order Lorentzians perform better. To get a more quantitative comparison, in panel (c) of Fig. 2 we study the mean-square error as a function of the number of basis elements used in the representation (and consequently in the SOP). In the panels (d)–(f) we consider the absolute difference between the exact moment, mean and variance of A and those obtained from the SOP. In all the graphs a basis made by second order Lorentzians is found to perform better.

In the present paper we considered up to 50 basis elements to avoid numerical noise that may originate in the NNLS fitting procedure. This limit depends strongly on the particular function to represent and on the degree of the Lorentzians used. In all the tests we found that the NNLS fit is more stable numerically with lower degree Lorentzians. This is probably due to the loss of smoothness in the basis set when the degree of the Lorentzians used is higher. In general, this numerical noise will produce instabilities in the algorithm if too many Lorentzians are used, and has to be controlled by careful numerical convergence studies on the target physical quantity (see also Sec. III C). On top of this, we can see that a saturation in the MSE is achieved around 40 basis elements in the case of second order Lorentzians and the convergence becomes slow. Although we did not performed a detailed study, we suspect this issue to be due to the constraint imposed on the amplitudes, which may be improved by modifying the NNLS algorithm.

It is worth noting that in order to represent the spectral function, here we use a NNLS minimization to get the coefficients (amplitudes) of the nth Lorentzian basis set. This results in having to solve a linear system of equations with a positive constraint on the solution. It is possible to improve on this via a nonlinear least squares minimization of center and broadening of the *n*th Lorentzians, i.e., optimizing also the basis and not only the coefficients.

III. APPLICATION: ONE-SHOT GW IN THE HEG FROM AIM-SOP

For validation, we apply the AIM-SOP approach to the paradigmatic case of the homogeneous electron gas (HEG), treated at the G_0W_0 level of theory [6,17,54]. Since we calculate propagators on the real axis we can easily access spectral (frequency-dependent) properties. The calculation of frequency-integrated ground-state quantities (occupation numbers, total energies, and thermodynamic quantities in general) can be obtained directly from the SOP representation of the spectral quantities computed in the procedure. While thermodynamic properties are usually obtained via additional calculations on the imaginary axis [26,33,55], in this paper spectral properties and integrated quantities are obtained simultaneously using the SOP representation of propagators computed on the real axis.

Although some quantities computed using the free-propagator G_0 have known analytical expressions, as is the case for the irreducible polarizability P_0 expressed via the Lindhard function [56,57], here we recompute explicitly all the quantities needed to evaluate the GW self-energy, making the treatment suitable also for self-consistent calculations. Therefore in the following the only assumption we make is to consider the initial Green's function as represented on SOP.

A. HEG propagators on the real frequency axis

In order to solve a one-shot $\mathrm{G_0W_0}$ cycle for the spin-unpolarized HEG, we first need to compute the irreducible polarizability at the independent-particle (or RPA) level, according to the integral

$$P(q,\omega) = 2\int \frac{d\mathbf{k}}{(2\pi)^3}\int \frac{d\omega'}{2\pi i}G(|\mathbf{k}+\mathbf{q}|,\omega+\omega')G(k,\omega'), \tag{24}$$

where $k = |\mathbf{k}|$ and $q = |\mathbf{q}|$ are the moduli of the electron and transferred quasimomentum, respectively. To compute Eq. (24), the frequency integral (convolution) is performed analytically according to Eq. (11). Then, we integrate numerically in spherical coordinates by performing the variable change $x = |\mathbf{k}+\mathbf{q}|$ on the azimuthal angle of $\mathbf{k}$,

$$P(q,\omega) = \frac{2}{q(2\pi)^2}\int_0^{+\infty} dk\, k \int_{|k-q|}^{|k+q|} dx\, x \times \int \frac{d\omega'}{2\pi i} G(x,\omega+\omega')G(k,\omega'), \tag{25}$$

which allows for the precalculation of the analytical convolutions on the two-dimensional (x, k) grid, instead of on the three-dimensional (k, q, θ) space. Exploiting the parity of $P(\omega)$, it is also possible to limit the $\mathbf{k}$ integration to the occupied states (see Appendix D). The numerical integration on the momentum is performed using the trapezoidal rule, which, despite its simplicity, ensures exponential convergence for decaying functions [58].

In order to have a SOP representation for the screened potential W we transform the polarizability $P(q,\omega)$ calculated on a frequency grid (at fixed momentum q) to a SOP performing a NNLS fitting, following the procedure detailed in Sec. II B. Then, we solve the Dyson equation using the algorithmic inversion for the polarizability (see Sec. II D) to obtain a SOP for W, and use it for the GW integral. An alternative possibility would be to solve the Dyson equation on a grid (which, due to homogeneity, is an algebraic inversion), and then represent W on SOP. Even admitting for an exact interpolation for the SOP of W on the calculated frequencies (where the Dyson equation is solved on grid), this SOP would suffer from not having solved the Dyson equation for all other frequencies. Instead, the SOP obtained from the algorithmic inversion comes from the exact solution of the Dyson equation at all frequencies (see Sec. II D). Conversely, this is not true for the grid inversion where the solution is exact only for isolated frequencies.

Concerning the self-energy integral

$$\Sigma(k,\omega) = \Sigma_x(k) + \frac{1}{(2\pi)^3}\int d\mathbf{q} \times \int_{-\infty}^{+\infty}\frac{d\omega'}{2\pi i} G(|\mathbf{k}+\mathbf{q}|,\omega+\omega')W_{\mathrm{corr}}(q,\omega'), \tag{26}$$

where $W_{\mathrm{corr}} = W - v_c$, we can still use Eq. (11) since we have the SOP representation of W. Again, in Eq. (26) we perform the $x = |\mathbf{k}+\mathbf{q}|$ change of variable obtaining

$$\Sigma(k,\omega) = \Sigma_x(k) + \frac{1}{k(2\pi)^2}\int_0^{+\infty} dq\, q \int_{|k-q|}^{|k+q|} dx \times \int \frac{d\omega'}{2\pi i} G(x,\omega+\omega')W_{\mathrm{corr}}(q,\omega'), \tag{27}$$

which allows for fewer convolutions (as for the polarizability integral), and use trapezoidal weights as in Eq. (25) for the momentum integration. The solution of the Dyson equation for the Green's function using the algorithmic inversion, and the calculation of frequency-integrated (thermodynamic) quantities, are discussed in the next section.

In Fig. 3 we show the overall flow chart describing the process of going from the knowledge of the initial Green's function to the calculation of the corresponding self-energy (for the HEG in the GW approximation), as implemented in the `heg_sgm.x` program of the `AGWX` suite [59], by means of the SOP approach. As opposed to the path in red, where the Dyson equations are solved on grids, in the green path we highlight the protocol followed in the present paper. The crucial difference between the two approaches is the use of the algorithmic-inversion method in order to solve exactly the Dyson equation.

B. Frequency-integrated quantities and thermodynamics

Having obtained the self-energy on a frequency grid following the procedure described in Sec. III A, the solution of the Dyson equation for the self-energy yields the Green's function of the system, while its frequency integration gives quantities like the occupation factor and the total energy. As mentioned, the SOP approach plays here a central role,

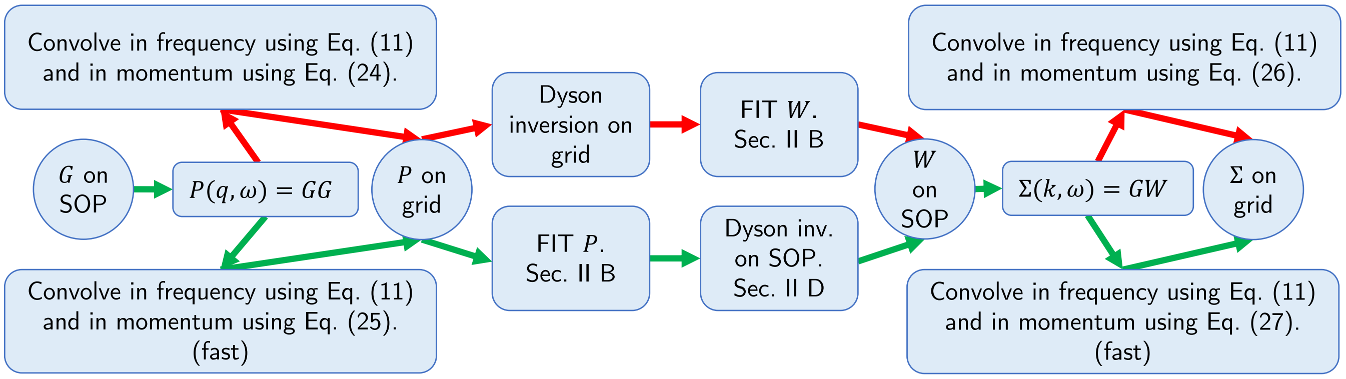

FIG. 3. Flow chart representing different strategies for the calculation of the self-energy given a Green's function G on SOP as input for the `heg_sgm.x` code. The strategy used in this article is highlighted with green lines.

enabling the possibility of performing analytical integrals for the moments of G, e.g., those involved in the Galitskii-Migdal expression for the total energy [see Eq. (28) below], and thus to have accurate thermodynamic (frequency-integrated) quantities. Moreover, the use of the algorithmic inversion allows for the exact solution of the Dyson equation for the Green's function at all frequencies. Indeed, the conservation of all sum rules (implied by the Dyson equation, see Sec. II) guaranteed by the AIM-SOP is fundamental when calculating the occupied moments of the spectral function.

As an example, the normalization condition of the spectral function is automatically satisfied when G on SOP is obtained using the algorithmic inversion, and allows for not having fitting constrains, which would be required, e.g., if we were to use a grid inversion. Moreover, the exact solution of the Dyson equation provided by the algorithmic inversion yields the equality between the renormalization factor Z calculated via the derivative of the self-energy at $k = k_f$ and $\omega = \epsilon_f$ with the value obtained using the discontinuity of the occupation factor n_k at $k = k_f$, given by the moment of the occupied spectral function.

In order to exploit the algorithmic-inversion method to get G represented as SOP, we obtain the SOP representation of the self-energy by performing a NNLS fitting of $\mathrm{Im}\Sigma(\omega)$ (see Sec. II B). Then, to compute the total energy from the knowledge of the Green's function G, we use the Galitski-Migdal expression [17,56] for the spin-unpolarized case,

$$\begin{aligned}\frac{E}{V} &= \int \frac{d\mathbf{k}}{(2\pi)^3}\left[\int_{-\infty}^{\mu} d\omega\, \omega A(k,\omega) + \frac{k^2}{2}\int_{-\infty}^{\mu} d\omega A(k,\omega)\right]\\ &= \int \frac{d\mathbf{k}}{(2\pi)^3}\left[\langle\epsilon_k\rangle + \frac{k^2}{2}n_k\right], \qquad (28)\end{aligned}$$

here in Hartree units. In this expression, the frequency integrals are performed using the SOP for G, and exploiting Eq. (12) with $m = 1$ and $m = 0$ for the first and second terms, respectively. Here n_k is the k-resolved occupation function, which sums to the total number of particles when integrated over momentum, and $\langle\epsilon_k\rangle$ is the occupied band energy, i.e., the first momentum of the occupied spectral function. In Fig. 4 we show the flow chart of the above procedure.

For both $m = 0$ and $m = 1$ moments, the equality between the moments of the Green's function and the moments of the occupied spectral function, Eqs. (12) and (B1), is assured by having used the algorithmic inversion when obtaining the SOP for the Green's function. Indeed, the knowledge of the self-energy on SOP and the use of the algorithmic inversion for solving exactly the Dyson equation ensures that the spectral function

$$A(\omega) = \frac{1}{\pi}\frac{|\mathrm{Im}\Sigma(\omega)|}{[\omega - \epsilon_0 - \mathrm{Re}\Sigma(\omega)]^2 + [\mathrm{Im}\Sigma(\omega)]^2}, \qquad (29)$$

decays at least as $\frac{\mathrm{Im}\Sigma}{\omega^2} = o(\omega^{-3})$, thereby making the first two occupied moments (see Sec. II C) converge. Additionally, even if we do not use the algorithmic inversion method to get G from Σ, the use of 2nd order Lorentzians from the representation of the spectral function A provides the identity between Eq. (12) and Eq. (B1), as the zeroth and first moments are well defined (see. Sec. II C for further reference).

Similarly to the discussion in Sec. III A, the SOP approach combined with the algorithmic inversion allows one to follow the workflow highlighted by the green path in Fig. 4. Overall, the results presented in Sec. IV are obtained using an implementation of the above approach in the `heg_sgm.x` program of the `AGWX` suite [59].

C. Numerical details

Here we discuss and report the parameters that control the numerical accuracy of the quantities (polarizability, self-energy, total energy) computed by means of Eqs. (25), (27), and (28). For the spectral quantities, this corresponds to going from left to right in the flow chart diagram of Fig. 3 following the green path, performing all calculations mentioned in the boxes. The first quantity to be computed is the polarizability $P(q,\omega)$. For each momentum q and frequency ω, we perform the integral of Eq. (25). We choose an initial free-particle Green's function having a 2nd order Lorentzian pole at each k broadened by δ_P. The k-momentum integral of Eq. (25) is limited by k_f (see Sec. III A), and we denote the spacing of the k and x grids by Δk_P and Δx_P, respectively. We call the spacing of the (q,ω) grid Δq and $\Delta\omega_P$ and build the q grid from 0 to $q^{\max}$ and the polarizability frequency grid from $[-\omega_P^{\max}, \omega_P^{\max}]$. Note that we will need to converge all the grid spacing parameters to zero, $\delta_P \to 0$, and $q^{\max}, \omega_P^{\max} \to \infty$. Due to the frequency-structure of the polarizability, for this

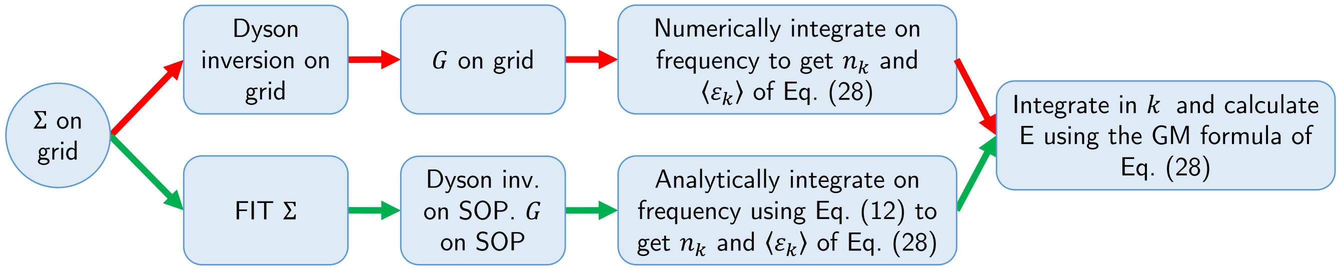

FIG. 4. Flow chart representing different strategies for the calculation of the total-energy given a self-energy Σ on a frequency grid as input for the `heg_sgm.x` code. The strategy used in this article is highlighted with green lines.

calculation it is best to pass in energy units which depend on the specific q point, following the law $f(q) = \sqrt{q} + q^2$. Thus, in these units the maximum of the frequency grid $\omega_P^{\max}$ scales with q, and specifically goes to 0 as $q \to 0$, and to infinity as $q \to \infty$. The scaling of the frequency grid allows for the polarizability to decay to 0 at the different momenta q, without having large frequency grids at small momenta, and was designed by looking at the ω/q dependence of the RPA-polarizability [e.g., from Eq. (C5) of Sec. C of the Appendix].

Moving to the central part of the flow chart in Fig. 3, the SOP representation of the polarizability is obtained following the method of Sec. II B, and placing the center of the 2nd order Lorentzians on the mid points of the frequency grid with a broadening equal to the spacing of the grid. With this choice, the accuracy of the fit improves as $\Delta\omega_P \to 0$. Next, we employ the algorithmic-inversion method to go from the SOP representation of the polarizability to the SOP of the screened-potential W. Using the SOP representation of W (and of G), the self-energy integral (right part of Fig. 3), Eq. (27), is formally identical to the integral in Eq. (25) for the polarizability. Therefore, the remaining parameters to converge are δ_Σ, Δx_Σ, Δk, $\Delta\omega_\Sigma$, $k^{\max}$, and $\omega_\Sigma^{\max}$ (using the same notation adopted above). As for the polarizability P, we obtain the SOP representation of the self-energy following Sec. II B, and placing the center of the 2nd order Lorentzians on the mid points of the frequency grid with a broadening equal to the spacing of the grid. Finally, we obtain the SOP representation of the Green's function employing the algorithmic-inversion method.

Using the resulting Green's function, we compute the thermodynamic quantities as detailed in Sec. III C, and study the numerical stability of the computational procedure with respect to all the above parameters. In this paper, we choose to converge the total energy, which is sensitive enough to guarantee a reasonable convergence for the other (spectral) properties of interest here. By changing individually each parameter (increase or decrease by 20% of its value towards convergence), we study the stability of the total energy against the selected parameter, keeping the values of all the others fixed at a reference point (baseline calculation of Fig. 5). Each target parameter is then converged separately until a plateau for the subsequent values of the computed quantity is observed. We evaluate the error on the result considering the two most distant values among those in the plateau.

Importantly, it is possible to reduce the number of parameters to converge from 13 to 5, by linking all the grid-spacing and broadening of the initial G_0 parameters together into a single variable, Δ, which ensures convergence for $\Delta \to 0^+$. Specifically, we bind those parameters together by setting $\Delta = \Delta k_P/k_f = 5\Delta x_P/k_f = \frac{1}{6}\Delta\omega_P/\epsilon_f = \frac{1}{9}\Delta q/k_f = \frac{1}{25}\Delta\omega_\Sigma/\epsilon_f = \Delta x_\Sigma/k_f = \frac{1}{3}\Delta k_\Sigma/k_f = \frac{5}{4}\delta_P/\epsilon_f = \frac{1}{100}\delta_\Sigma/\epsilon_f$. Together with Δ, the grid-limit parameters are converged separately, following the strategy designed above. The converged values obtained for all the calculated densities are: $\Delta = 0.00133$, $q^{\max} = 7.292\ k_f$, $k^{\max} = 3.60\ k_f$, $\omega_P^{\max} = 5.0\ \epsilon_f$, $\omega_\Sigma^{\max} = 10.985\ \epsilon_f$, where k_f is the Fermi momentum and ϵ_f the Fermi energy. To give a sense of how many poles are needed in our approach—recalling that the number of poles are equal to the number of points in the frequency mesh times the degree of the Lorentzians—we highlight that at convergence we use for the polarizability and screened potential $2 \times \frac{\omega_P^{\max}}{\delta_P} \approx 2400$ poles, and for the self-energy $2 \times \frac{\omega_\Sigma^{\max}}{\delta_\Sigma} \approx 660$ poles. Furthermore, the most of the computational time is spent performing the convolutions of Eqs. (25) and (27), even if a linear scaling in the number of poles of the propagators is implied by exploiting Eq. (11).

As a last point, we stress that all our calculations are performed with the electron-electron self-energy shifted by μ, i.e., $G(k,\omega) = [\omega - \epsilon_k^0 - \Sigma(k,\omega) + \mu]^{-1}$. This choice translates in having all energy scales aligned with the chemical

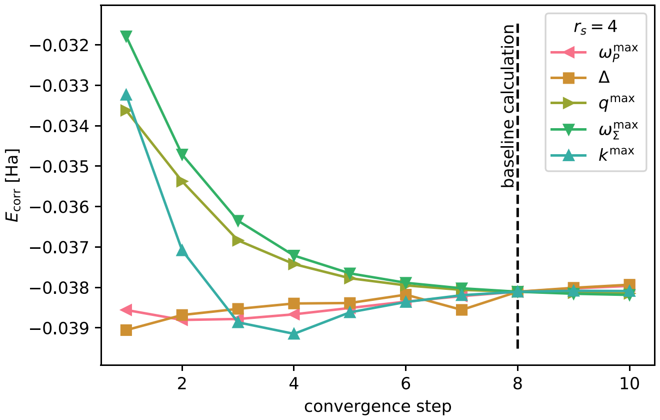

FIG. 5. Convergence study for the correlation energy per particle E_{corr} from a G_0W_0 calculation for the HEG at $r_s = 4$. The parameters to converge are described in Sec. III C. For each convergence curve (represented by a single line), we study the value of E_{corr} by varying the corresponding parameter, fixing all the others at the convergence point (called baseline calculation). At each step, we vary the target parameter by 20% in the convergent direction and observe a plateau in E_{corr}.

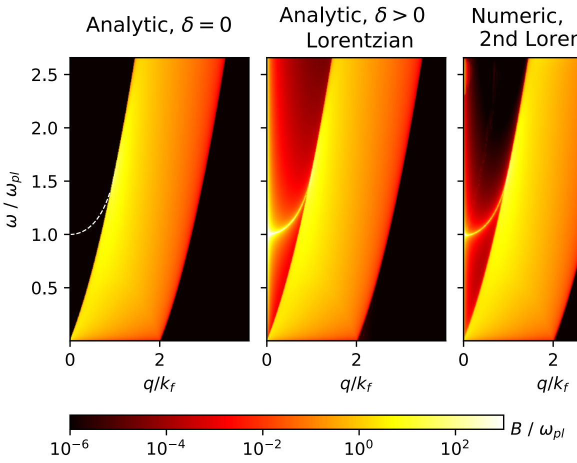

FIG. 6. Imaginary part (divided by π and taken without sign) of the screened potential of the HEG at $r_s = 4$ in a one-shot G_0W_0 calculation. Momenta are in units of the Fermi momentum and energies in units of the plasma frequency of the gas at the specified density. The color map is logarithmic, and the values $<10^{-6}$ and $>10^{3}$ are mapped to 10^{-6} and 10^{3}, respectively. Left panel: Analytic result at zero broadening ($\delta = 0$). The functional form for the color plot is taken from Ref. [61]. The plasmonic band (dashed line) is calculated numerically, see Sec. IV A for details. Central panel: Analytic result at finite (Lorentzian) broadening ($\delta = 10^{-5}\ \epsilon_f$), see Sec. C of the Appendix for details. Right panel: Numerical results obtained using SOPs with 2nd order Lorentzians, see Sec. IV A for details.

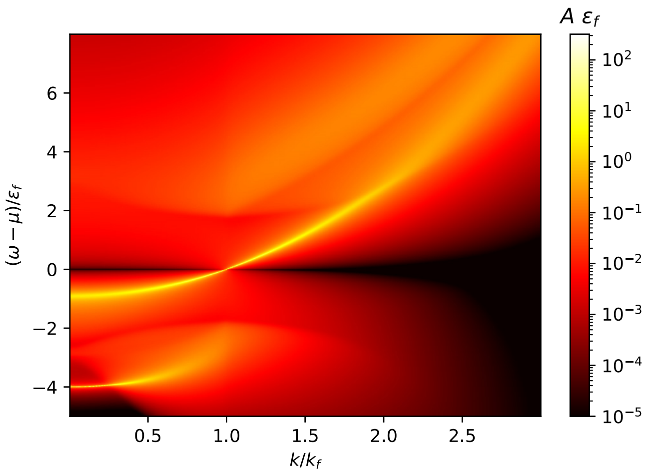

FIG. 7. Spectral function of the HEG at $r_s = 4$ from a G_0W_0 calculation. The Fermi energy is $\epsilon_f = \frac{k_f^2}{2m_e}$ with k_f the Fermi momentum. $\mu = \epsilon_f(1 - 0.0545)$ is the chemical potential. The scale of the color-map is logarithmic.

potential for all propagators, and in particular that $\Sigma(k_f, \omega = 0)$ means to evaluate the self-energy at $k = k_f$ and at the chemical potential. In this sense, we can define the chemical potential μ as $\mu = \epsilon_f + \Sigma(k_f, 0)$, and update it after the G_0W_0 cycle. This manual shift for μ originates from the non-self-consistent nature of a G_0W_0 calculation and helps to conserve the number of particles and the analytic structure of the propagator G, including, e.g., the analytic divergence of the spectral function A at $k = k_f$ and $\omega = \mu$. A similar approach is also used in Refs. [39,41,60].

IV. RESULTS

In this section we discuss the results obtained applying the SOP approach to the case of the one-shot G_0W_0 calculation in the HEG. First, we extensively discuss the $r_s = 4$ case, also one of the most studied in the literature, and then in Sec. IV C we provide results for more densities ranging from $r_s = 1$ to $r_s = 10$.

A. Spectral propagators on the real axis

We start by considering the screened potential $W(q, \omega)$ computed at the G_0 level. In Fig. 6 we compare the imaginary part of W (divided by π and taken without sign), calculated following the procedure described in Sec. III B (right panel), with its analytic expressions at zero broadening ($\delta = 0$, left panel) and at finite Lorentzian broadening ($\delta = 10^{-5}\ \epsilon_f$, center panel). While for $\delta = 0$ the analytic expression for the polarizability (and consequently for W) is well known [61], at finite δ the derivation of an analytic time-ordered form for W (thus for W) is given in Sec. C of the Appendix. Notice that at $\delta = 0$ the plasmonic band for small q vectors (dashed line) has to be calculated numerically since coming from a set of delta functions [62]. Here, we obtain it for $q/k_f < 1$ by numerically finding the roots of the plasmonic equation (e.g., Eq. 15.11 of Ref. [61]), using the analytic form for the polarizability at zero broadening.

Overall, from the plot comparison we can qualitatively infer that the SOP approach, together with its numerical implementation, is working effectively in computing and representing the dynamical screened potential across a range of different values of q. The plot also shows that W calculated numerically using second order Lorentzians for G_0 ($\delta = 0.000741\ \epsilon_f$) is sharper then the analytic form with a simple Lorentzian broadening ($\delta = 10^{-5}\ \epsilon_f$), though δ is smaller in the latter case. This further stresses that the use of 2nd order Lorentzians for G_0 can be seen as a convergence accelerator to the $\delta \to 0$ limit (see Sec. II A).

Next, we look at the self-energy numerical procedures by examining directly the G_0W_0 spectral function as shown in Fig. 7. This is done computing the integral in Eq. (27), representing the self-energy on SOP with 2nd order Lorentzians, using the algorithmic inversion for the self-energy, and then evaluating the Green's function on a frequency grid. Focusing the attention on the lower satellite as well as on the quasiparticle band, we can see that Fig. 7 compares well with Refs. [30,62] (note that, at variance with Ref. [30], we use a logarithmic scale to represent the intensity of the spectral function, in order to highlight its structure). The plasmaron peak [62] is very visible for small momenta where the quasiparticle band broadens, while the satellite band in the occupied-frequency range ($\omega < \mu$) is sharper. Vice versa, as k approaches k_f, the plasmaron broadens, and the quasiparticle band becomes more peaked. At $k = k_f$ the spectral function presents the typical metallic divergence along the quasiparticle band, while occupied and empty satellites are almost of the same weight (see also Fig. 9 for details of the spectral functions at selected k), in agreement with Ref. [39]. For

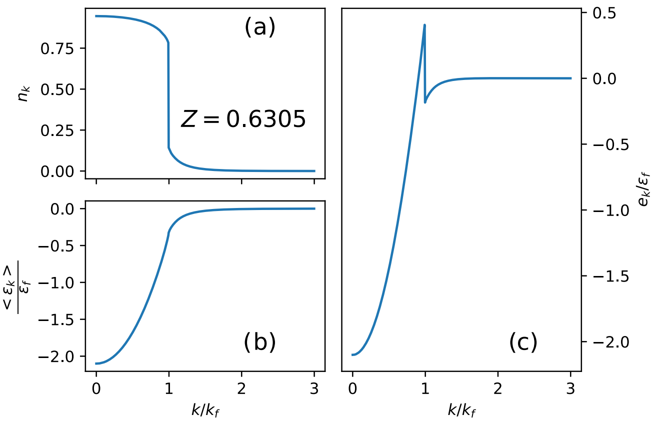

FIG. 8. Selected frequency integrated quantities from a G_0W_0 calculation of the HEG at $r_s = 4$. Panel (a): The occupation number in arbitrary units as a function of the momentum k together with the renormalization factor (discontinuity of n_k). Panel (b): The occupied band energy $\langle \epsilon_k \rangle$ as a function of k (see Sec. III B for details). Panel (c): The Galitzki-Migdal total-energy resolved over k contributions e_k, according to the rhs of Eq. (28) as function of the momentum k. k_f and ϵ_f are the Fermi momentum and energy respectively.

$k > k_f$ satellites coming from empty states ($\omega > \mu$) become dominant along with the quasiparticle band.

B. Frequency integrated quantities and thermodynamics

We now discuss the resulting frequency-integrated quantities from the spectral function obtained in the previous section. Being the HEG a metal, the use of the algorithmic-inversion method to get a spectral function that obeys all sum rules (implied by the Dyson equation, see Sec. II D for details), including, e.g., the correct normalization, is crucial for obtaining well-converged results. For example, the Luttinger discontinuity of n_k makes the value of the total energy from the Galitzki-Migdal very sensitive to the converging parameters, thus requiring very accurate computations.

The converged value for the correlation energy—total energy minus Fock-exchange—extrapolated from Fig. 5 at $r_s = 4$ is 0.0381 ± 0.0003 Ha, in agreement with Refs. [26] (with a difference of 0.0003 Ha), where calculations were done along the imaginary axis. In panel (a) of Fig. 8 we plot the occupation number n_k, and in panel (b) the occupied band energy $\langle \epsilon_k \rangle$ (defined in Sec. III B). The occupation number n_k presents a sharp Luttinger discontinuity, which indicates that the broadening used in Eq. (27) is well controlled and does not spoil the quality of the results. The renormalization factor in panel (a) $Z = 0.6305$, calculated using the frequency derivative of the self-energy on SOP at $k = k_f$ and $\omega = \epsilon_f$ (see Sec. III for details), compares well with Refs. [39,41,43,63] (where we extrapolate Z from the graphs when necessary).

In panel (c) of Fig. 8 we plot the total-energy resolved over k contributions e_k [rhs of Eq. (28)]. As previously mentioned, due to the presence of the Luttinger discontinuity, this function is sharp and thus difficult to integrate, at variance, e.g., with the RPA-Klein-energy functional, which is expected to be smoother [64]. Additionally, we made attempts to obtain the total energy via a frequency-grid (brute-force) strategy to perform the integral of Eq. (28), but we found the grid-spacing parameter to be critical. We accounted for this numerical instability as due to the nonsmooth structure of the spectral function, especially near the chemical potential at k_f, where it has a discontinuity. Nevertheless, in Refs. [65,66] the authors obtain an accurate frequency integration of the GM formula on the real axis, with results in very good agreement with this work and with the already cited literature.

C. G_0W_0 for a broad range of HEG densities

In this section we report the results for the HEG with r_s ranging from 1 to 10 studied at the G_0W_0 level, following the same approach used for $r_s = 4$. In Fig. 9 we show the computed data for the spectral function obtained with the AIM-SOP approach for specific momenta k and densities ($r_s = 2, 4$). For $k = 0$, we take the actual grid point $k = 0.0028 k_f$ since the exact zero point is forbidden in our implementation of Eq. (27). At the available momenta $k/k_f = 0.5$, 1.0, and 1.5, and density $r_s = 4$, the spectral functions compares qualitatively well with Refs. [39,41].

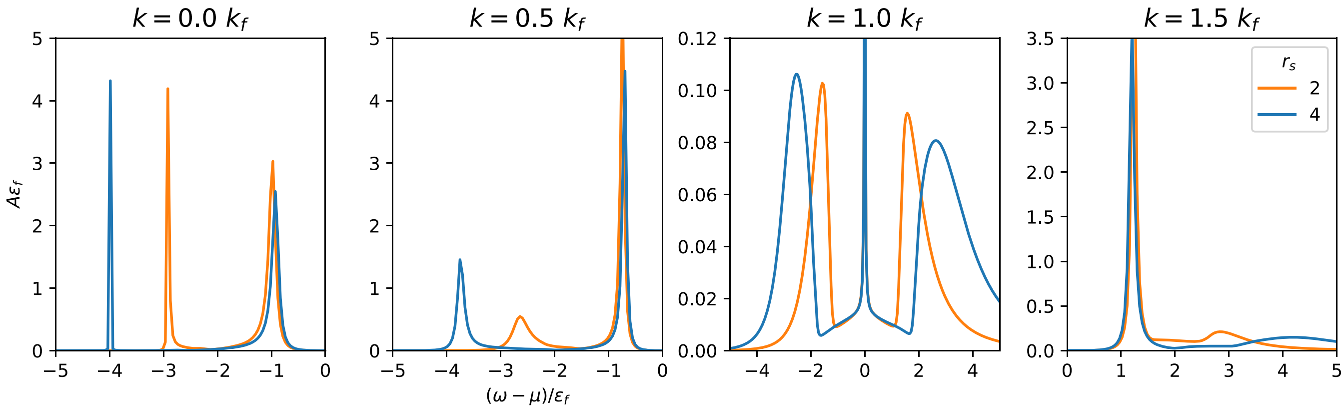

FIG. 9. Spectral functions of the HEG at selected k points (indicated on top) for $r_s = 2$ and $r_s = 4$. Energies are in units of ϵ_f and momenta of k_f.

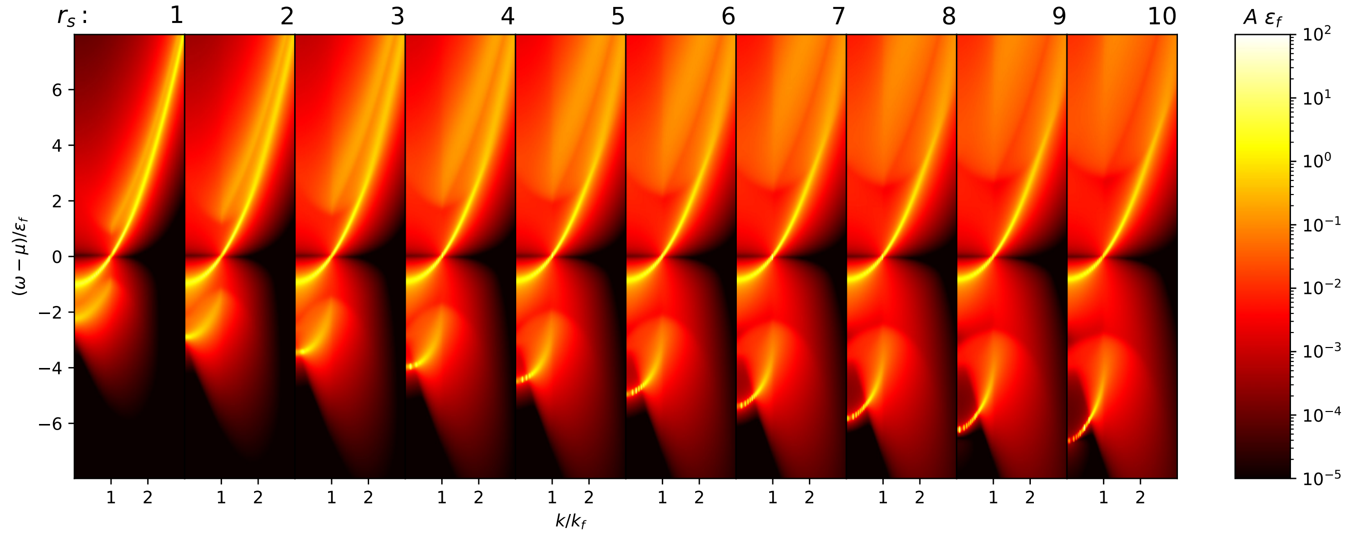

FIG. 10. Spectral functions of the HEG at several densities. At the top r_s specifies the density. The Fermi energy is $\epsilon_f = \frac{\hbar^2 k_f^2}{2m_e}$ with k_f the Fermi momentum. μ is the chemical potential. The color map is logarithmic.

In Fig. 10 we show the computed data for the spectral function at all momenta and frequencies obtained with the AIM-SOP approach. In the chosen units (ϵ_f for the energy and k_f for the momentum) the spectral function for increasing r_s shows an increase in the separation between the quasiparticle band and the satellite occupied and empty bands. Indeed, in these units r_s controls the interaction strength—see Eq. (3.24) of Ref. [61]—with the limits of the noninteracting gas obtained for $r_s \to 0$ and the strongly interacting gas corresponding to $r_s \to \infty$. Accordingly, the plasmaron peak of the satellite band at small momenta is weakened for smaller r_s. The same behaviours can be observed in the occupation factors of Fig. 11 for the different densities. For $r_s \to 0$ the HEG approaches the noninteracting limit and the occupation number drops from 1 to 0 at k_f. Going towards $r_s = 10$ the jump becomes smaller, since the quasiparticle is reduced due to the more evident satellite bands, as it can be seen in Fig. 10.

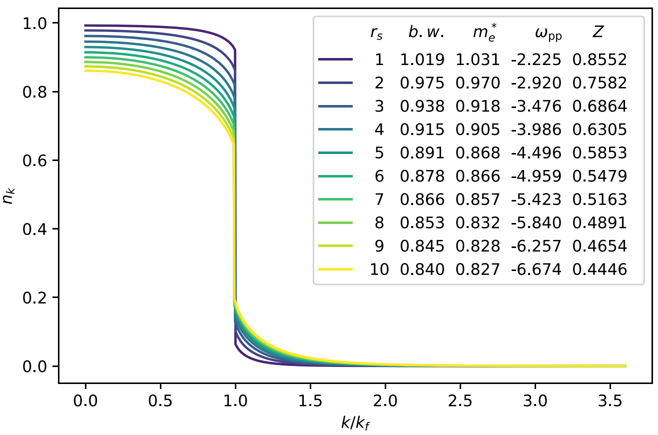

r_s	$b.w.$	m_e^*	ω_{pp}	Z
1	1.019	1.031	-2.225	0.8552
2	0.975	0.970	-2.920	0.7582
3	0.938	0.918	-3.476	0.6864
4	0.915	0.905	-3.986	0.6305
5	0.891	0.868	-4.496	0.5853
6	0.878	0.866	-4.959	0.5479
7	0.866	0.857	-5.423	0.5163
8	0.853	0.832	-5.840	0.4891
9	0.845	0.828	-6.257	0.4654
10	0.840	0.827	-6.674	0.4446

FIG. 11. Occupation factors in arbitrary units for several densities (r_s from 1 to 10). k_f is the Fermi momentum. In the inset we display the band width $b.w.$ in units of ϵ_f, the effective mass m_e^* in units of $2m_e$, the plasmaron frequency ω_{pp} in units of ϵ_f, and the renormalization factor in arbitrary units at each density.

The resulting renormalization factors Z are displayed in the last column of the inset of Fig. 11 and compare well with the literature [63]. In the inset of Fig. 11 we also show the band width ($b.w.$), effective mass (m_e^*), and plasmaron frequency (ω_{pp}) at each density.[1]

In Table I we report the corresponding total energies computed at the different densities, together with some of the available results in the literature. Also, results that are not explicitly reported in Table I, e.g., from Refs. [65,66], are in overall very good agreement. Since calculations in Ref. [26] were done on the imaginary axis, we shall consider those as the most accurate for the comparison. We refer to Sec. E of the Appendix, for the convergence studies of the total energies for the different densities. We find at $r_s = 1$ the largest discrepancy (0.0059 Ha) with respect to the data of Ref. [26]. This can be rationalized by noting, e.g., that n_k is a steeper function, thereby enhancing the numerical issues of the Galitzki-Migdal expression discussed in Sec. III B. To deepen the understanding of this numerical discrepancy, aside the convergence study of Fig. 14 provided in the Appendix, we performed an additional calculation increasing the refinement parameter Δ by 20%, aiming at increasing the accuracy in the integral grids, to target the steeper character of $r_s = 1$. The result, 0.0736 Ha (against 0.0749 Ha of Table I), is acceptable considering the error of 0.0015 Ha reported in the Table. Most importantly we stress that at variance with Ref. [26], our procedure provides not only accurate frequency-integrated

---

[1] We calculate band width ($b.w.$), effective mass (m_e^*), and plasmaron frequency (ω_{pp}) from the spectral function on the (k, ω) grid at each density, using a simple algorithm to find maxima of the function at fixed momentum. At $k = 0$, starting the local optimization from $\omega = -10\epsilon_f$, the plasmaron peak ω_{pp} is found. The quasiparticle band is obtained collecting from the different momenta k the optimization results, each started at $\omega = 0$. This is then fitted using a symmetric parabola (for $k < 0.6k_f$) to estimate the curvature (effective mass, m_e^*) and the y intercept (band width, $b.w.$).

TABLE I. Correlation energies as function of r_s for the HEG at the G_0W_0 level. Energies are in Hartree units.

	HEG: G_0W_0 Correlation Energies $\lvert E_{\mathrm{corr}}\rvert$		
r_s	This paper	Ref. [42]	Ref. [26]
1	0.0749 (±0.0015)	0.0722	0.0690
2	0.0545 (±0.0003)	0.0539	0.0530
3	0.0451 (±0.0008)	0.0448	
4	0.0381 (±0.0003)	0.0382	0.0378
5	0.0333 (±0.0002)	0.0355	0.0331
6	0.0297 (±0.0002)		
7	0.0268 (±0.0002)		
8	0.0245 (±0.0002)		
9	0.0226 (±0.0002)		
10	0.0210 (±0.0002)		0.0207

quantities (e.g., the total energy), but also precise spectral properties on the real axis (key quantities for spectroscopy).

In Fig. 12 we plot the correlation energy of Table I as a function of r_s, including the Perdez-Zunger (PZ) fit of the quantum Monte Carlo (QMC) Ceperley Alder data as a reference [67,68]. We also exploit the same functional form of PZ to fit our data, providing in Table II γ, β_1, and β_2 for the fitting function of the correlation energy in the HEG (in Hartree),

$$E_{\mathrm{corr}}(r_s) = \frac{\gamma}{1+\beta_1\sqrt{r_s}+\beta_2 r_s}, \tag{30}$$

together with the covariance matrix of the fit. In Fig. 12 we plot the result of the fit as a green line. Given the fit accuracy in Table II, this may be considered as an effective parametrization of the G_0W_0 correlation energy of the electron gas.

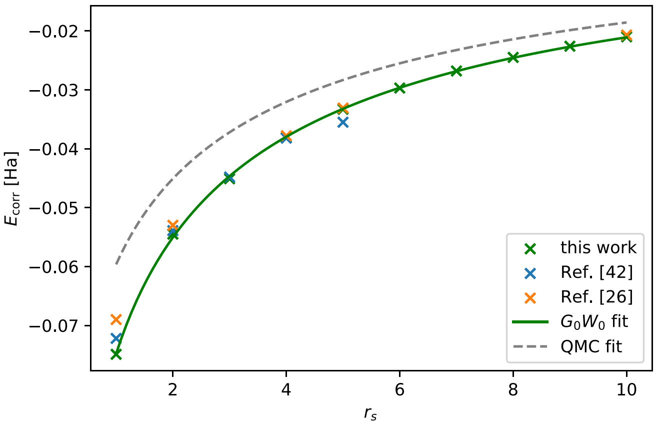

FIG. 12. Correlation energy in Hartree units for several densities within the G_0W_0 approximation in the HEG. The data found in this paper are marked using green crosses. In blue we show the results from Ref. [42], and in orange from Ref. [26]. In solid green we plot the correlation energy fit from Eq. (30) (same functional form as in [67]) on the present (green) data. For reference, in dashed grey we add also the quantum Monte Carlo data obtained by Ceperley and Alder [68] using the fit made by Perdew and Zunger [67].

TABLE II. Parameters of the correlation energy fit in Hartree, Eq. (30) (same functional form as in [67]), using the data of Table I, and the covariance matrix of the fit. The fitted function is plotted in Fig. 12.

γ	β_1	β_2
−0.1929	1.1182	0.4609
	Covariance matrix of the fit	
0.00022	−0.00277	−0.00011
	0.03497	0.00123
		0.00014

V. CONCLUSIONS

In this paper, after introducing a sum-over-poles (SOP) representation for propagators, we present the novel algorithmic-inversion method (AIM-SOP) to solve Dyson-like equations and handle frequency-dependent quantities in dynamical theories. Specializing to the case of many-body perturbation theory, we show that the AIM-SOP is able to provide a unified formalism for spectral and thermodynamic properties of an interacting-electron system. Expanding all frequency-dependent quantities on SOP, we use the AIM-SOP to solve exactly and at all frequencies Dyson-like equations, getting analytic frequency-dependent (spectral) and frequency-integrated (thermodynamic) properties. This is allowed by the mapping of the Dyson equation to an effective Hamiltonian of dimension controlled by the number of poles in the SOP of the self-energy (see Sec. II D). The transformation of frequency-dependent quantities into SOP is performed exploiting the representation of their spectral functions on different basis sets: Aside from the standard choice of a basis of Lorentzians, we introduce nth order generalized Lorentzian basis elements (see Sec. II A) with improved decay properties. This allows for better numerical stability when transforming a propagator to SOP (see Sec. II B), improved analytic properties for calculating the thermodynamic quantities (see Sec. II C), and an acceleration of convergence to the thermodynamic limit (zero broadening and infinite k-space sampling). Also, once the SOP representation of a propagator is known, we use the Cauchy residue theorem to calculate convolutions and (occupied) moments, accessing both spectral and thermodynamic quantities (see Sec. II C).

In order to have a working example of the AIM-SOP approach, we apply it to the paradigmatic case of many-body perturbation theory at the G_0W_0 level for the HEG at several densities (r_s from 1 to 10). Using the AIM-SOP, we are able to provide accurate spectra simultaneously with precise frequency-integrated quantities (e.g., occupation numbers and total energies). At the available densities, we find very good agreement with Refs. [30,62] for the spectral function. Moving to the total energy, we provide an in depth study of the stability and convergence of our results, finding quantitative agreement with Ref. [26] for the available r_s, where calculations are performed on the imaginary axis.

Although in this paper we study a homogeneous system as test case, the AIM-SOP approach aims to treat realistic nonhomogeneous systems in the more general framework of dynamical embedding theories. Relevant aspects include a full-frequency representation of potentials and propagators, the flexibility for self-consistent calculations, and the exact solution of Dyson-like equations. Besides the extension to spatial degrees of freedom for the algorithmic inversion, we believe that improving on the dynamical representation of propagators is also an interesting course for future research.

ACKNOWLEDGMENTS

We acknowledge stimulating discussions with Dario A. Leon. This work was supported by the Swiss National Science Foundation (SNSF) through Grant No. 200021-179138 (T.C.) and its National Centre of Competence in Research MARVEL on "Computational Design and Discovery of Novel Materials" (N.M.), and from the "MAterials design at the eXascale–European Centre of Excellence" (MaX), funded by the European Union program H2020-INFRAEDI-2018-1 under Grant No. 824143 (N.M., A.F.).

APPENDIX A: SUM-OVER-POLES REPRESENTATION OF AN n-th ORDER LORENTZIAN

In this Appendix we obtain the SOP representation of a Green's function featuring a spectral function described by a single nth order Lorentzian. Recalling Sec. II A, the discrete time-ordered Hilbert transform [Eq. (5)] of a (not normalized) nth order Lorentzian centered in ϵ_j and broadened by δ_j,

$$\int \frac{d\omega'}{\pi}\frac{1}{\omega-\omega'-i0^+\,\mathrm{sgn}(\mu-\epsilon_j)}\frac{|\delta_j|^{2n-1}}{(\omega'-\epsilon_j)^{2n}+(\delta_j)^{2n}}, \tag{A1}$$

induces a SOP representation for the Green's function, see Sec. II A. The expression in Eq. (A1) can be computed explicitly using the residue theorem. Closing the contour in the lower/upper plane for $\epsilon_j \lessgtr \mu$, the poles of the integrand

$$\zeta_{j,m} = \epsilon_j + e^{i\frac{\pi}{2n}(1+2m)}\delta_j \tag{A2}$$

come only from the spectral function A. Using L'Hôpital's rule, the residues of the integrand are reduced to

$$R_{j,m} = -\frac{1}{2n\pi}\frac{e^{i\frac{\pi}{2n}(1+2m)}}{\omega-\zeta_{j,m}-i0^+\,\mathrm{sgn}(\epsilon_j)}. \tag{A3}$$

Thus, taking the limit for $\mathcal{C}$ on the real axis, residues and poles of the SOP for G are those in Eqs. (9) and (10). The normalization of the nth order Lorentzian is given by summing all the α_m from Eq. (9) and using the geometric sum,

$$N_n = -\frac{i}{n}\sum_{m=0}^{n-1} e^{i\frac{\pi}{2n}(1+2m)} = \frac{1}{n\sin\left(\frac{\pi}{2n}\right)}. \tag{A4}$$

APPENDIX B: MOMENTS OF A PROPAGATOR AND OCCUPIED MOMENTS OF ITS SPECTRAL FUNCTION

In this Appendix we discuss the equality between the (regularized) moments of a propagator, defined in Eq. (12), and the occupied moments of its spectral function. For simplicity of notation we restrict to the case of a spectral function A composed by a single nth Lorentzian $\mathcal{L}^n_{\delta_j}$, as defined in Eq. (7), and focus on the case $m \leqslant 2(n-1)$:

$$\begin{aligned}E_m[G] &= \oint_\Gamma \frac{dz}{2\pi i}\int d\omega\,\frac{e^{iz0^+}z^m\mathcal{L}_{\delta_j}(\omega-\epsilon_j)}{z-\omega-i0^+\,\mathrm{sgn}(\mu-\epsilon_j)}\\ &= \int d\omega\,\mathcal{L}_{\delta_j}(\omega-\epsilon_j)\\ &\quad\times\oint_\Gamma \frac{dz}{2\pi i}\frac{e^{iz0^+}z^m}{z-\omega-i0^+\,\mathrm{sgn}(\mu-\epsilon_j)}\\ &= \int_{-\infty}^{+\infty} d\omega\,\omega^m\mathcal{L}_{\delta_j}(\omega-\epsilon_j)\theta(\mu-\epsilon_j),\end{aligned} \tag{B1}$$

where Γ is defined as in Eq. (12) and the integral on the last line is well defined since $\mathcal{L}_{\delta_j} \sim \frac{1}{\omega^{2n}}$ for large frequencies, and $m \leqslant 2(n-1)$. Also, the integrals extend over the whole real axis because we are dealing with a single basis element (a single n-th Lorentzian), taken here as retarded. Time-ordering is accounted for by the $\theta(\mu-\epsilon_j)$ factors. In fact, in the continuum limit of a complete basis representation (defined in Sec. II A) the last line of Eq. (B1) becomes $\int_{-\infty}^{\mu} d\omega\,\omega^m A(\omega)$. For the higher order moments, $m > 2(n-1)$, the above equalities are not valid, with the rhs of Eq. (12) becoming complex, and the last line of Eq. (B1) diverging. While the diverging of the rhs of Eq. (B1) can be understood by looking at the decay of the overall integral, the imaginary contribution to the moment of Eq. (12) may be seen explicitly by inserting residues and poles of $\mathcal{L}^n_{\delta_j}$ from Eqs. (9) and (10), and using the binomial expansion. In summary, Eq. (12) can be rewritten as

$$E_m[G] = \frac{1-e^{\frac{i\pi}{2}}}{2}\sum_{k=0}^{m}\binom{m}{k}\epsilon_j^{m-k}\delta_j^k e^{\frac{i\pi k}{2n}}\sum_{p=0}^{n-1}e^{\frac{i\pi(k+1)}{n}p}, \tag{B2}$$

which is in general complex, and reduces the real number

$$E_m[G] = \frac{1}{nN_n}\sum_{\substack{k=0\\ \text{even}}}^{m}\binom{m}{k}\epsilon_j^{m-k}\delta_j^k\left[\sin\frac{\pi(k+1)}{2n}\right]^{-1}, \tag{B3}$$

if $m \leqslant 2(n-1)$. In the case of $m > 2(n-1)$, we can still use Eq. (12) to calculate the occupied moment, and improve on the result by lowering the broadening of the Lorentzian(s), which in turn reduces the spurious imaginary part of the targeted moment.

APPENDIX C: TIME-ORDERED G_0G_0 POLARIZABILITY AT FINITE (LORENTZIAN) BROADENING

In this Appendix we calculate the time-ordered G_0G_0 polarizability at finite (Lorentzian) broadening δ. Note that usually, e.g., in Ref. [61], the calculation is carried out at $\delta = 0$. Starting from Ref. [61] before the $\eta \to 0^+$ limit is taken, P^0 reads:

$$\begin{aligned}P^0(q,\omega) = \frac{2}{(2\pi)^3}\int d^3k\,&\frac{\theta(|\mathbf{q}+\mathbf{k}|-k_f)\theta(k_f-k)}{\omega+\epsilon_k-\epsilon_{|\mathbf{k}+\mathbf{q}|}+i\eta}\\ &-\frac{\theta(k_f-|\mathbf{q}+\mathbf{k}|)\theta(k-k_f)}{\omega+\epsilon_k-\epsilon_{|\mathbf{k}+\mathbf{q}|}-i\eta}.\end{aligned} \tag{C1}$$

Measuring the momenta in units of k_f, the energies in units of ϵ_f, and exploiting the free-particle energy dispersion $\epsilon_k =$

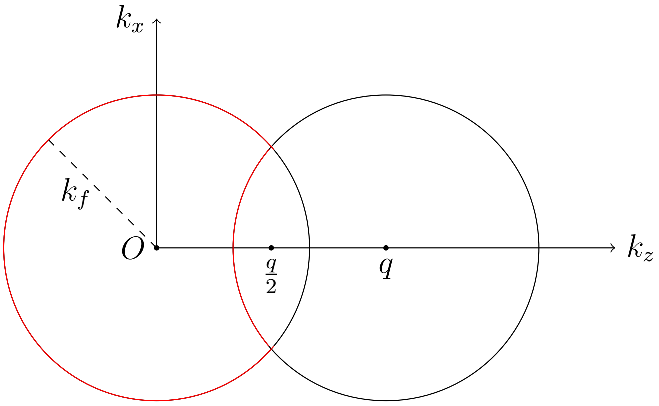

FIG. 13. 2D-projection of Ω onto the (k_z, k_y) plane. Ω can be seen as the volume of revolution around the k_z axis of the region delimited by the red line.

k^2, it is possible to rewrite the first addend of Eq. (C1) as

$$I(q,z) = \frac{1}{2q}\int_{\Omega} d^3k\,\frac{1}{z+k_z}, \tag{C2}$$

assuming a the reference system with q along the k_z axis and $z = \frac{\omega}{2q} - \frac{q}{2} + i\frac{\eta}{q}$. The integral domain Ω can be seen as the volume of revolution around the k_z axis of the region delimited by the red line in Fig. 13. We calculate I by integrating over the whole sphere ($\Omega_{\rm sph}$) of radius k_f and then subtracting the remainder part ($\Omega_{\rm R}$). The result on the whole sphere is

$$I_{\Omega_{\rm sph}}(q,z) = \frac{2\pi}{q}\left(\frac{z}{2} + \frac{1-z^2}{4}\ln\frac{z+1}{z-1}\right), \tag{C3}$$

and for the remainder part it reads:

$$\begin{aligned} I_{\Omega_{int}}(q,z) = \frac{\pi}{2q}\Bigg[&\left(1-\frac{q}{2}\right)(2z+q) \\ &- ((z+q)^2-1)\ \log\left(\frac{z+q/2}{z+q-1}\right) \\ &- (z^2-1)\log\left(\frac{z+1}{z+q/2}\right)\Bigg]. \end{aligned} \tag{C4}$$

Observing that the second addend in Eq. (C1) can be obtained by changing the sign of the frequency ω in the first, the expression for the G_0G_0 polarizability is

$$\begin{aligned} P^0(q,\omega) = \frac{4k_f m_e}{(2\pi)^3\hbar}\Bigg[&I\left(\frac{\omega/\epsilon_f}{2q/k_f} - \frac{q/k_f}{2} + i\frac{\eta/\epsilon_f}{q/k_f}\right) \\ &+ I\left(\frac{-\omega/\epsilon_f}{2q/k_f} - \frac{q/k_f}{2} + i\frac{\eta/\epsilon_f}{q/k_f}\right)\Bigg], \end{aligned} \tag{C5}$$

where $I = I_{\Omega_{\rm sph}} - I_{\Omega_{\rm R}}$. In addition, the analytic continuation of this function can be done substituting the real ω with a complex one.

APPENDIX D: EXPLOITING PARITY OF THE RPA-POLARIZABILITY INTEGRAL

In this Appendix we show how it is possible to exploit the parity of the polarizability $P(q,\omega)$ at fixed momentum $\mathbf{q}$. As explained in Sec. II C, the SOP approach allows to compute analytically the convolution of Eq. (24). Using Eq. (11) in Eq. (24), the polarizability may be rewritten as

$$\begin{aligned} P(q,\omega) = 2\int \frac{d\mathbf{k}}{(2\pi)^3} \\ \times \Bigg[&\sum_{\substack{i,j \\ \mathrm{Im}\{z_i(|\mathbf{k}+\mathbf{q}|)\}<0 \\ \mathrm{Im}\{z_j(k)\}>0}} \frac{A_i(|\mathbf{k}+\mathbf{q}|)A_j(k)}{\omega + z_j(k) - z_i(|\mathbf{k}+\mathbf{q}|)} \\ &- \sum_{\substack{i,j \\ \mathrm{Im}\{z_i(|\mathbf{k}+\mathbf{q}|)\}>0 \\ \mathrm{Im}\{z_j(k)\}<0}} \frac{A_i(|\mathbf{k}+\mathbf{q}|)A_j(k)}{\omega + z_j(k) - z_i(|\mathbf{k}+\mathbf{q}|)}\Bigg], \end{aligned} \tag{D1}$$

where we did not yet restrict to the G_0 case in which only one pole is present. Defining $I(|\mathbf{k}+\mathbf{q}|_{\rm unocc}, k_{\rm occ}, \omega)$ the first term in the rhs ($k_{\rm occ}$ labels the occupied states with momentum k, while $|\mathbf{k}+\mathbf{q}|_{\rm unocc}$ refers to empty states), and setting $\mathbf{k}+\mathbf{q} \to -\mathbf{k}$ in the second term,

$$\begin{aligned} P(q,\omega) = 2\int \frac{d\mathbf{k}}{(2\pi)^3}\,&[I(|\mathbf{k}+\mathbf{q}|_{\rm unocc}, k_{\rm occ}, \omega) \\ &+ I(|\mathbf{k}+\mathbf{q}|_{\rm unocc}, k_{\rm occ}, -\omega)], \end{aligned} \tag{D2}$$

it is possible to limit the calculation to the first term. Specializing to the case of $G = G_0$ of Sec. III A, the occupied states at momentum k are all within the Fermi sphere, and thus we can limit the momentum integration to the sphere of radius k_f, i.e., $k \leqslant k_f$ in Eqs. (24) and (25).

APPENDIX E: TOTAL ENERGY CONVERGENCE STUDIES FOR SEVERAL DENSITIES OF THE HEG

In Fig. 14 we report the convergence studies obtained for the total energy at all the densities following the protocol detailed in Sec. III C. We omit the density corresponding at $r_s = 4$ since already treated in the main text. Similar considerations to the $r_s = 4$ case can be drawn for these cases.

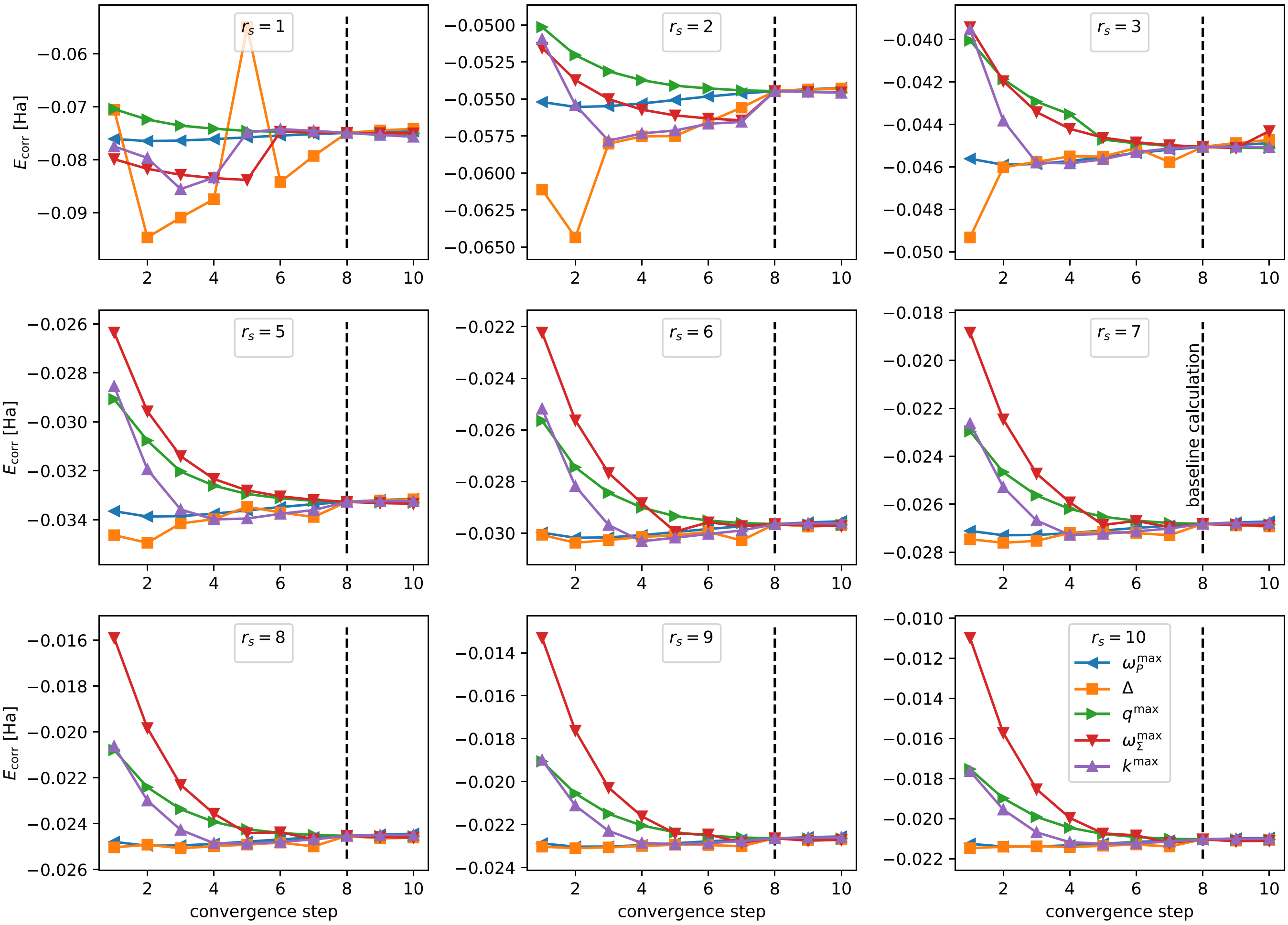

FIG. 14. Convergence studies for the total energy at $r_s = \{1, 2, 3, 5, 6, 7, 8, 9, 10\}$ following the protocol detailed in Sec. III C.

---

[1] N. Marzari, A. Ferretti, and C. Wolverton, Electronic-structure methods for materials design, Nat. Mater. **20**, 736 (2021).

[2] J. Hafner, C. Wolverton, and G. Ceder, Toward computational materials design: The impact of density functional theory on materials research, MRS Bull. **31**, 659 (2006).

[3] S. Curtarolo, G. L. W. Hart, M. B. Nardelli, N. Mingo, S. Sanvito, and O. Levy, The high-throughput highway to computational materials design, Nat. Mater. **12**, 191 (2013).

[4] N. Mounet, M. Gibertini, P. Schwaller, D. Campi, A. Merkys, A. Marrazzo, T. Sohier, I. E. Castelli, A. Cepellotti, G. Pizzi, and N. Marzari, Two-dimensional materials from high-throughput computational exfoliation of experimentally known compounds, Nat. Nanotechnol. **13**, 246 (2018).

[5] J. S. Zhou, L. Reining, A. Nicolaou, A. Bendounan, K. Ruotsalainen, M. Vanzini, J. J. Kas, J. J. Rehr, M. Muntwiler, V. N. Strocov, F. Sirotti, and M. Gatti, Unraveling intrinsic correlation effects with angle-resolved photoemission spectroscopy, Proc. Natl. Acad. Sci. USA **117**, 28596 (2020).

[6] L. Reining, The GW approximation: Content, successes and limitations, WIREs Comput. Mol. Sci. **8**, e1344 (2018).

[7] H. Ma, M. Govoni, and G. Galli, Quantum simulations of materials on near-term quantum computers, npj Comput. Mater. **6**, 1 (2020).

[8] H. Ma, N. Sheng, M. Govoni, and G. Galli, Quantum embedding theory for strongly correlated states in materials, J. Chem. Theory Comput. **17**, 2116 (2021).

[9] R. Van Noorden, B. Maher, and R. Nuzzo, The top 100 papers, Nat. News **514**, 550 (2014).

[10] P. Hohenberg and W. Kohn, Inhomogeneous electron gas, Phys. Rev. **136**, B864 (1964).

[11] M. Levy, Universal variational functionals of electron densities, first-order density matrices, and natural spin-orbitals and solution of the *v*-representability problem, Proc. Natl. Acad. Sci. USA **76**, 6062 (1979).

[12] J. P. Perdew, K. Burke, and M. Ernzerhof, Generalized Gradient Approximation Made Simple, Phys. Rev. Lett. **77**, 3865 (1996).

[13] J. Sun, A. Ruzsinszky, and J. Perdew, Strongly Constrained and Appropriately Normed Semilocal Density Functional, Phys. Rev. Lett. **115**, 036402 (2015).

[14] A. J. Cohen, P. Mori-Sánchez, and W. Yang, Insights into current limitations of density functional theory, Science **321**, 792 (2008).

[15] J. P. Perdew, W. Yang, K. Burke, Z. Yang, E. K. U. Gross, M. Scheffler, G. E. Scuseria, T. M. Henderson, I. Y. Zhang, A. Ruzsinszky, H. Peng, J. Sun, E. Trushin, and A. Görling, Understanding band gaps of solids in generalized Kohn-Sham theory, Proc. Natl. Acad. Sci. USA **114**, 2801 (2017).

[16] N. L. Nguyen, N. Colonna, A. Ferretti, and N. Marzari, Koopmans-Compliant Spectral Functionals for Extended Systems, Phys. Rev. X **8**, 021051 (2018).

[17] R. M. Martin, L. Reining, and D. Ceperley, *Interacting Electrons Theory and Computational Approaches* (Cambridge University Press, Cambridge, 2016).

[18] A. Georges, G. Kotliar, W. Krauth, and M. J. Rozenberg, Dynamical mean-field theory of strongly correlated fermion systems and the limit of infinite dimensions, Rev. Mod. Phys. **68**, 13 (1996).

[19] A. A. Kananenka, E. Gull, and D. Zgid, Systematically improvable multiscale solver for correlated electron systems, Phys. Rev. B **91**, 121111(R) (2015).

[20] T. N. Lan and D. Zgid, Generalized self-energy embedding theory, J. Phys. Chem. Lett. **8**, 2200 (2017).

[21] A. Calzolari, N. Marzari, I. Souza, and M. Buongiorno Nardelli, *Ab initio* transport properties of nanostructures from maximally localized Wannier functions, Phys. Rev. B **69**, 035108 (2004).

[22] A. Ferretti, A. Calzolari, B. Bonferroni, and R. D. Felice, Maximally localized Wannier functions constructed from projector-augmented waves or ultrasoft pseudopotentials, J. Phys.: Condens. Matter **19**, 036215 (2007).

[23] L. Hedin, J. Michiels, and J. Inglesfield, Transition from the adiabatic to the sudden limit in core-electron photoemission, Phys. Rev. B **58**, 15565 (1998).

[24] A. Damascelli, Z. Hussain, and Z.-X. Shen, Angle-resolved photoemission studies of the cuprate superconductors, Rev. Mod. Phys. **75**, 473 (2003).

[25] D. Golze, M. Dvorak, and P. Rinke, The GW Compendium: A practical guide to theoretical photoemission spectroscopy, Front. Chem. **7**, 377 (2019).

[26] P. García-González and R. W. Godby, Self-consistent calculation of total energies of the electron gas using many-body perturbation theory, Phys. Rev. B **63**, 075112 (2001).

[27] A. Schindlmayr, P. García-González, and R. W. Godby, Diagrammatic self-energy approximations and the total particle number, Phys. Rev. B **64**, 235106 (2001).

[28] N. E. Dahlen and U. v. Barth, Variational energy functionals tested on atoms, Phys. Rev. B **69**, 195102 (2004).

[29] N. E. Dahlen, R. van Leeuwen, and U. von Barth, Variational energy functionals of the Green function and of the density tested on molecules, Phys. Rev. A **73**, 012511 (2006).

[30] Y. Pavlyukh, G. Stefanucci, and R. van Leeuwen, Dynamically screened vertex correction to *GW*, Phys. Rev. B **102**, 045121 (2020).

[31] A. L. Kutepov, Electronic structure of Na, K, Si, and LiF from self-consistent solution of Hedin's equations including vertex corrections, Phys. Rev. B **94**, 155101 (2016).

[32] B. Farid, R. Daling, D. Lenstra, and W. van Haeringen, *GW* approach to the calculation of electron self-energies in semiconductors, Phys. Rev. B **38**, 7530 (1988).

[33] H. N. Rojas, R. W. Godby, and R. J. Needs, Space-Time Method for *Ab Initio* Calculations of Self-Energies and Dielectric Response Functions of Solids, Phys. Rev. Lett. **74**, 1827 (1995).

[34] A. L. Kutepov and G. Kotliar, One-electron spectra and susceptibilities of the three-dimensional electron gas from self-consistent solutions of Hedin's equations, Phys. Rev. B **96**, 035108 (2017).

[35] D. A. Leon, C. Cardoso, T. Chiarotti, D. Varsano, E. Molinari, and A. Ferretti, Frequency dependence in *GW* made simple using a multipole approximation, Phys. Rev. B **104**, 115157 (2021).

[36] R. Levy, J. P. F. LeBlanc, and E. Gull, Implementation of the maximum entropy method for analytic continuation, Comput. Phys. Commun. **215**, 149 (2017).

[37] R. N. Silver, D. S. Sivia, and J. E. Gubernatis, Maximum-entropy method for analytic continuation of quantum Monte Carlo data, Phys. Rev. B **41**, 2380 (1990).

[38] G. F. Giuliani and G. Vignale, *Quantum Theory of the Electron Liquid* (Cambridge University Press, Cambridge, 2005).

[39] U. von Barth and B. Holm, Self-consistent GW_0 results for the electron gas: Fixed screened potential W_0 within the random-phase approximation, Phys. Rev. B **54**, 8411 (1996).

[40] B. Holm and F. Aryasetiawan, Self-consistent cumulant expansion for the electron gas, Phys. Rev. B **56**, 12825 (1997).

[41] B. Holm and U. von Barth, Fully self-consistent *GW* self-energy of the electron gas, Phys. Rev. B **57**, 2108 (1998).

[42] B. Holm and F. Aryasetiawan, Total energy from the Galitskii-Migdal formula using realistic spectral functions, Phys. Rev. B **62**, 4858 (2000).

[43] B. I. Lundqvist, Single-particle spectrum of the degenerate electron gas. I, Phys. Kondens. Mater. **6**, 193 (1967).

[44] B. I. Lundqvist, Single-particle spectrum of the degenerate electron gas. II, Phys. Kondens. Mater. **6**, 206 (1967).

[45] B. I. Lundqvist, Single-particle spectrum of the degenerate electron gas, Phys. Kondens. Mater. **7**, 117 (1968).

[46] G. E. Engel, B. Farid, C. M. M. Nex, and N. H. March, Calculation of the *GW* self-energy in semiconducting crystals, Phys. Rev. B **44**, 13356 (1991).

[47] M. Abramowitz and I. A. Stegun (eds.), *Handbook of Mathematical Functions with Formulas, Graphs and Mathematical Tables* (Dover Publications, New York, 1965).

[48] P. Virtanen, R. Gommers, T. E. Oliphant, M. Haberland, T. Reddy, D. Cournapeau, E. Burovski, P. Peterson, W. Weckesser, J. Bright *et al.*, SciPy 1.0: Fundamental algorithms for scientific computing in Python, Nat. Methods **17**, 261 (2020).

[49] C. L. Lawson and R. J. Hanson, *Solving Least Squares Problems*, Classics in Applied Mathematics, SIAM (Prentice-Hall, Englewood Cliffs, 1995).

[50] K.-H. Lee and K. J. Chang, Analytic continuation of the dynamic response function using an *N*-point Padé approximant, Phys. Rev. B **54**, R8285 (1996).

[51] G. B. Thomas and M. D. Weir, *Calculus and Analytic Geometry* (Addison-Wesley, Reading, MA, 1988).

[52] S. Y. Savrasov, K. Haule, and G. Kotliar, Many-Body Electronic Structure of Americium Metal, Phys. Rev. Lett. **96**, 036404 (2006).

[53] S. J. Bintrim and T. C. Berkelbach, Full-frequency GW without frequency, J. Chem. Phys. **154**, 041101 (2021).

[54] F. Aryasetiawan and O. Gunnarsson, The *GW* method, Rep. Prog. Phys. **61**, 237 (1998).

[55] M. M. Rieger, L. Steinbeck, I. D. White, H. N. Rojas, and R. W. Godby, The *GW* space-time method for the self-energy of large systems, Comput. Phys. Commun. **117**, 211 (1999).

[56] A. L. Fetter and J. D. Walecka, *Quantum Theory of Many-Particle Systems* (McGraw-Hill, New York, 1971).

[57] G. Giuliani and G. Vignale, *Quantum Theory of the Electron Liquid* (Cambridge University Press, Cambridge, 2005).

[58] L. N. Trefethen and J. A. C. Weideman, The exponentially convergent trapezoidal rule, SIAM Rev. **56**, 385 (2014).

[59] T. Chiarotti and S. Vacondio, and A. Ferretti, `AGWX` code suite.

[60] H. O. Frota and G. D. Mahan, Band tails and bandwidth in simple metals, Phys. Rev. B **45**, 6243 (1992).

[61] A. L. Fetter and J. D. Walecka, *Quantum Theory of Many-particle Systems* (Courier Corporation, New York, 2003).

[62] F. Caruso and F. Giustino, The GW plus cumulant method and plasmonic polarons: Application to the homogeneous electron gas, Eur. Phys. J. B **89**, 238 (2016).

[63] Y. Dewulf, D. Van Neck, and M. Waroquier, Discrete approach to self-consistent GW calculations in an electron gas, Phys. Rev. B **71**, 245122 (2005).

[64] C.-O. Almbladh, U. V. Barth, and R. V. Leeuwen, Variational total energies from phi- and psi- derivable theories, Int. J. Mod. Phys. B **13**, 535 (1999).

[65] J. J. Kas, J. J. Rehr, and L. Reining, Cumulant expansion of the retarded one-electron Green function, Phys. Rev. B **90**, 085112 (2014).

[66] M. Z. Mayers, M. S. Hybertsen, and D. R. Reichman, Description of quasiparticle and satellite properties via cumulant expansions of the retarded one-particle Green's function, Phys. Rev. B **94**, 081109(R) (2016).

[67] J. P. Perdew and A. Zunger, Self-interaction correction to density-functional approximations for many-electron systems, Phys. Rev. B **23**, 5048 (1981).

[68] D. M. Ceperley and B. J. Alder, Ground State of the Electron Gas by a Stochastic Method, Phys. Rev. Lett. **45**, 566 (1980).